Geophysical Journal International

Geophys. J. Int. (2013) doi: 10.1093/gji/ggt155

Geophysical Journal International Advance Access published May 22, 2013

Kinematic fault slip evolution source models of the 2008 M7.9 Wenchuan earthquake in China from SAR interferometry, GPS and teleseismic analysis and implications for Longmen Shan tectonics

Eric J. Fielding,[1] Anthony Sladen,[2,*] Zhenhong Li,[3] Jean-Philippe Avouac,[2] Roland Bürgmann[4] and Isabelle Ryder[4,†]

[1]*Jet Propulsion Laboratory, California Institute of Technology,* 4800 *Oak Grove Drive, MS* 300-233, *Pasadena, CA* 91109, *USA. E-mail: eric.j.fielding@jpl.nasa.gov*

[2]*Tectonics Observatory, California Institute of Technology, Mail Code* 100-23, 1200 *California Boulevard, Pasadena, CA* 91125, *USA*

[3]*School of Geographical and Earth Sciences, University of Glasgow, Glasgow* G12 8QQ, *UK*

[4]*Department of Earth and Planetary Science,* 389 *McCone Hall, University of California, Berkeley, CA* 94720-4767

Accepted 2013 April 15. Received 2013 March 1; in original form 2012 June 1

SUMMARY

The M_w 7.9 2008 Wenchuan earthquake ruptured about 280 km of faults in the Longmen Shan of Sichuan province, China, at the eastern edge of the Tibetan Plateau. We use teleseismic waveforms with geodetic data from Global Positioning System, synthetic aperture radar interferometry and image amplitude correlation to produce a source model of this earthquake. The model describes evolution of fault slip during the earthquake. The geodetic data constrains the spatial distribution of fault slip and the seismic waveforms constrain mostly the time evolution of slip. We find that the earthquake started with largely thrust motion on an imbricate system of faults beneath the central Longmen Shan, including the Beichuan Fault and Pengguan Fault, with fault slip at depth extending up to 50 km northwest of the mountain front. The fault ruptures continued northeast along the Beichuan Fault with more oblique slip (right-lateral and thrust) and the proportion of lateral motion increasing in the northern Longmen Shan. The northernmost fault segment has a much steeper dip, consistent with nearly pure strike-slip motion. The kinematic source model shows that the rupture propagated to the northeast at about 2.5–3.0 km s^{-1}, producing a cascade of subevents with a total duration of about 110 s. The complex fault ruptures caused shortening and uplift of the extremely steep central Longmen Shan, which supports models where the steep edge of the plateau is formed by thrusting over the strong crust of the Sichuan Basin.

Key words: Radar interferometry; Earthquake source observations; Seismicity and tectonics; Body waves; Continental tectonics: compressional.

1 INTRODUCTION

The eastern margin of the Tibetan Plateau is marked by a steep mountain front called the Longmen Shan where elevations drop abruptly from an average of about 4500 m in the eastern plateau to about 500 m in the Sichuan basin to the east (Fig. 1). This area is the steepest edge of the Tibetan Plateau (Fielding 1996; Liu-Zeng *et al.* 2011). However, while the other steep edges are sustained by rapid active thrusting with rates typically larger than 1 cm yr^{-1}, the shortening rate across the Longmen Shan measured from geodesy is small, less than a few mm yr^{-1} (Chen *et al.* 2000; Shen *et al.* 2005; Burchfiel *et al.* 2008; Zhang *et al.* 2008) and consistent with low long-term erosion rates of 0.1–1 mm yr^{-1} (Godard *et al.* 2010) and the absence of a well-developed foreland basin (Burchfiel *et al.* 1995). There is no doubt that active thrusting is taking place there, as shown from morphotectonic studies (Densmore *et al.* 2007), structural interpretation of seismic profiles and surface geology (Hubbard & Shaw 2009) and not least the devastating M_w 7.9 Wenchuan earthquake which is the focus of this study.

The earthquake occurred on 2008 May 12 beneath the Longmen Shan mountain front in the Sichuan province of China. The earthquake epicentre was located in Wenchuan County and the rupture continued into Beichuan County, where damage to the city of Beichuan was extreme. The earthquake caused great damage extending almost 300 km along the Longmen Shan and adjacent areas.

* Now at: Geoazur, Observatoire de la Côte d'Azur, Université de Nice – Sophia Antipolis, CNRS, IRD, Bat. 4, 250 rue Albert Einstein, 06560 Valbonne, France.

† Now at: School of Environmental Sciences, 4 Brownlow Street, University of Liverpool, Liverpool L36 3GP, UK.

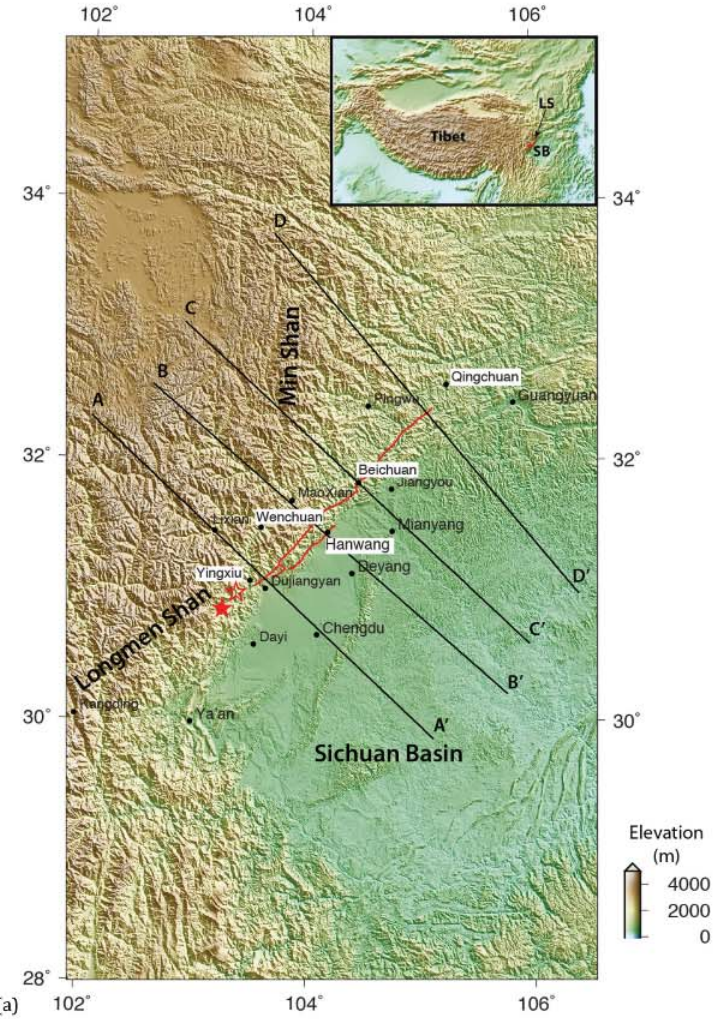

Figure 1. (a) Topographic map of the Longmen Shan and adjacent Tibetan plateau and Sichuan basin, derived from GMTED2010 7.5-arcsecond spacing mean elevations (Danielson & Gesch 2011). Inset shows location of Longmen Shan (LS) and Sichuan Basin (SB) relative to the Tibetan Plateau. Open red star marks May 12, 2008 M7.9 USGS epicentre, solid red star shows epicentre used in our slip evolution models, and red lines show surface ruptures. Black lines show centres of swath profiles in Fig. 17. (b) Areas covered by SAR image pairs used in the fault slip analysis (Table 2). Track numbers label each swath. Black lines outline Envisat image mode swaths; blue lines are ALOS PALSAR fine-beam swaths. Red outline of lavender polygon shows extent of Envisat ScanSAR interferogram. Green lines outline ALOS PALSAR ScanSAR interferogram. (c) Topographic map of extended area around the Longmen Shan and Sichuan Basin with overlay of GPS interseismic velocities and their 50 per cent confidence ellipses (Shen *et al.* 2005). Solid black lines are major faults from Replumaz & Tapponnier (2003) and red lines are surface ruptures of 2008 earthquake.

Many groups mapped the surface ruptures in the field and measured the fault offsets at a number of locations (e.g. Xu *et al.* 2008a,b; Liu-Zeng *et al.* 2009). Field mapping showed that the main surface rupture occurred on a thrust fault that has been called the Beichuan Fault, and there was also significant slip on a subparallel thrust fault system called the Pengguan Fault (Xu *et al.* 2008a,b; Liu-Zeng *et al.* 2009). Both of these faults were identified as active before the earthquake (Densmore *et al.* 2007).

A number of previous studies have already documented this earthquake based on field observations of surface ruptures (mentioned above), the measurement of surface deformation from GPS or remote-sensing and seismology (Kobayashi *et al.* 2009; Shen *et al.* 2009; de Michele *et al.* 2010b; Feng *et al.* 2010; Furuya *et al.* 2010; Tong *et al.* 2010; Xu *et al.* 2010; Wang *et al.* 2011; Zhang *et al.* 2011; Wen *et al.* 2012). Here we build on these previous studies by assembling a larger synthetic aperture radar (SAR) and GPS data set, which provides constraints on static coseismic deformation, and analysing these data together with seismological records of the earthquake's rupture. We present a kinematic analysis of the temporal evolution of slip on the coseismic fault ruptures, and discuss implications for the long-term deformation that has formed and maintained this plateau edge.

2 DATA SETS

We combine three types of data in this study, GPS measurements of coseismic offsets of ground stations, SAR data from two satellites, and seismic waves recorded on the global seismic network (GSN). We use the fully-processed GPS displacements from Wang *et al.* (2011), including both the horizontal and vertical components, in

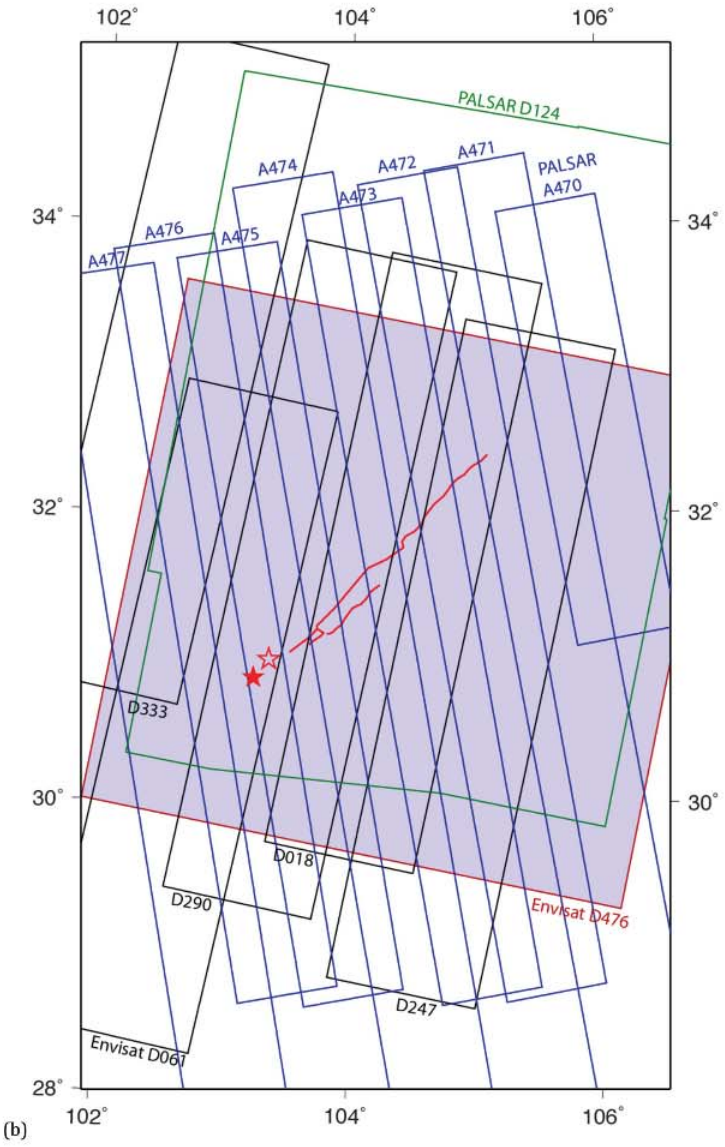

Figure 1. (*Continued.*)

our slip evolution and total coseismic fault slip inversions. Most of the GPS data were collected in campaign mode, so the coseismic offsets include up to four weeks of post-seismic deformation (Working Group of the Crustal Motion Observation Network of China Project 2008; Shen *et al.* 2009; Wang *et al.* 2011). We also use levelling data from Wang *et al.* (2009) as an independent check on our models, but don't include them in the kinematic inversions. In this section, we provide details on the SAR and seismological data, which we additionally used in this study.

2.1 SAR data processing

The SAR data were acquired by the JAXA (Japanese Aerospace Exploration Agency) Advanced Land Observation Satellite (ALOS) and the ESA (European Space Agency) Envisat satellite. The Envisat data are effective in the low-relief areas with less vegetation in the Sichuan Basin and further into the Tibetan Plateau, but are not so useful in the steep and vegetated Longmen Shan. The ALOS phased-array L-band SAR (PALSAR) was operational until 2011 and acquired data with a 23.8 cm radar wavelength, which usually provides better interferometric coherence in areas of vegetation than shorter radar wavelengths, including the C-band (5.6 cm) wavelength used by the Envisat advanced SAR (ASAR). We used both the high-resolution stripmap imagery [PALSAR fine beam (FB) and ASAR image mode (IM)] and the moderate-resolution ScanSAR imagery (scanning SAR, PALSAR wideswath burst mode 1, WB1 and ASAR wide-swath, WS) in our analysis.

All SAR data from the ALOS and Envisat satellites were processed from the raw signal data (Level 1.0 for PALSAR and Level 0 for ASAR). Nine pairs of PALSAR acquisitions with up to 13 frames per date (see Table 1) and eight pairs of ASAR scenes (see Table 2) were analysed. This is the most complete set of

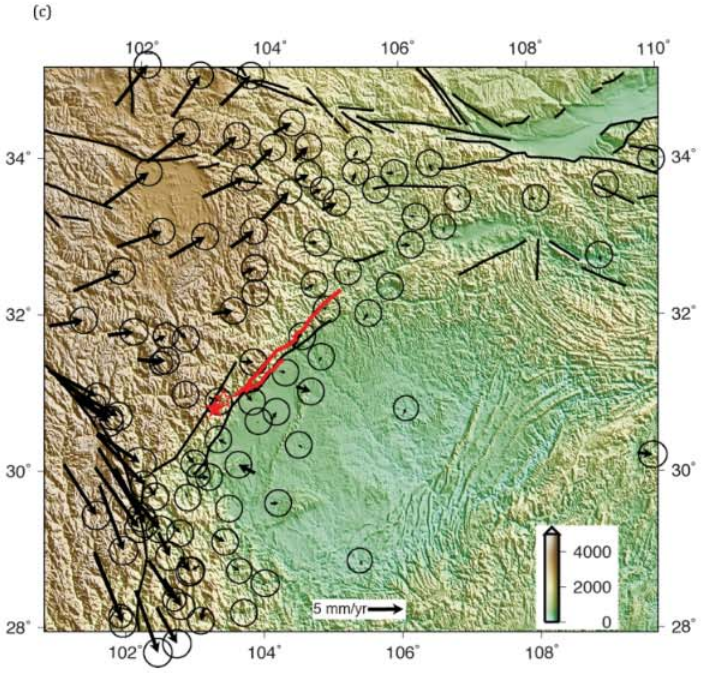

Figure 1. (*Continued.*)

Table 1. Details of ALOS PALSAR interferograms. Columns show ALOS path, satellite direction (ascending or descending), pre-earthquake date (month/day/year), post-earthquake date, perpendicular component of the baseline at the centre of the start of the interferogram (centre of subswath 4 for path 124 ScanSAR interferogram), perpendicular component at the end of the interferogram, PALSAR frames processed and imaging mode (FB is fine beam or stripmap; WB is wide beam or ScanSAR mode).

Path	Direction	Pre date	Post date	Bperp start m	Bperp end m	Frames	Mode
470	asc.	9/27/07	6/29/08	−878	−982	610–660	FB
471	asc.	2/29/08	5/31/08	38	128	550–670	FB
472	asc.	1/28/07	6/17/08	191	212	570–680	FB
473	asc.	2/17/08	5/19/08	179	273	570–660	FB
474	asc.	3/5/08	6/5/08	245	330	540–660	FB
475	asc.	6/20/07	6/22/08	−2	−76	590–620	FB
476	asc.	4/8/08	5/24/08	−213	−178	570–660	FB
477	asc.	4/25/08	6/10/08	−86	−69	550–650	FB
124	desc.	1/3/08	5/20/08	847	708	2950–3000	WB1

Table 2. Details of Envisat ASAR interferograms. Columns show Envisat track (all are descending direction), pre-earthquake date (month/day/year), post-earthquake date, perpendicular component of the baseline at the centre of the start of the interferogram, perpendicular component at the end of the interferogram, imaging mode (imaging mode beam 2, IM2 or wide-swath, WS) and burst synchronization for ScanSAR (wide-swath) interferograms.

Track	Pre date	Post date	Bperp start m	Bperp end m	Mode	Burst sync. Per cent
333	11/22/07	6/19/08	62	90	IM2	
61	7/21/07	5/31/08	−3	3	IM2	
290	8/6/07	6/16/08	216	242	IM2	
18	12/15/04	5/28/08	111	162	IM2	
247	11/16/07	8/22/08	−162	−180	IM2	
247[a]	1/25/08	6/13/08	83		WS	86
476	7/15/07	6/29/08	84		WS	93
204[a]	1/22/08	5/24/08	−208		WS	96

[a]Not used in slip inversions.

interferometric SAR data analysed and published to date for this event. For each pair, we used the first SAR acquisition in the same mode after the earthquake to minimize the amount of post-seismic deformation included and the pre-quake image was selected to optimize the interferometric coherence by minimizing the spatial and temporal separation of the orbits, with the additional constraint of burst alignment for ScanSAR pairs. The pairs include between 7 and 102 days of time after the earthquake (Table 2). The high-resolution FB PALSAR and IM ASAR images, acquired in stripmap modes, were processed with the JPL/Caltech ROI_pac interferometric SAR (InSAR) package (Rosen *et al.* 2004). The wide-swath (WS) ASAR images, acquired in ScanSAR mode, were processed with the commercial SARmap SARscape package. The wide-swath burst mode 1 (WB1) PALSAR images, also ScanSAR, were processed using the technique of adding zero lines to make faux stripmap data described by Tong *et al.* (2010) and then using ROI_pac for the rest of the processing. We used a version of the Shuttle Radar Topography Mission (SRTM) 3-arcsecond (90 m) spacing digital elevation model (DEM) that has the voids filled with other data sources (Jarvis *et al.* 2008, available from http://srtm.csi.cgiar.org), which we call SRTM-CIATv4. The central part of the Longmen Shan had very large voids in the original SRTM-3 version 2 released by NASA (Farr *et al.* 2007) and the alternative data have lower accuracy but allow processing of the full SAR scenes.

2.2 SAR pixel tracking

In addition to the InSAR analysis (described in more detail below), which provides measurements of surface displacements in the radar line-of-sight (LOS) direction with a precision of a small fraction of the radar wavelength where the interferograms are coherent, pixel offset tracking was also applied to the FB PALSAR and IM ASAR image pairs. Pixel offset tracking, or sub-pixel correlation of the SAR backscatter amplitude images, can be used to measure displacements to a precision of a fraction of the SAR pixel size in both the radar LOS and along the satellite track with a spatial resolution of several hundred metres (Michel *et al.* 1999; Pathier *et al.* 2006; Kobayashi *et al.* 2009; de Michele *et al.* 2010a). The cross-correlations for the pixel tracking were performed on the full-resolution, single-look complex SAR images, using matching windows of 64 × 64 pixels using ROI_pac. The topographic component of the LOS offsets was removed using the SRTM-CIATv4 DEM. The pixel offset tracking is much less precise than InSAR measurements but it can measure the very large displacements close to the fault ruptures. We used the pixel offset maps to determine the locations of the Wenchuan earthquake surface ruptures shown in Fig. 1 by picking the large discontinuities in the offsets. We tried some slip inversions using the pixel offset maps but they did not improve the results, largely because our simplified fault geometry cannot match the complex fault geometry near the surface that causes strong variations in ground displacements close to the faults. Our pixel offset results are similar to those in Kobayashi *et al.* (2009) and de Michele *et al.* (2010b).

The LOS (slant-range) pixel offset maps extracted from the ALOS PALSAR data have better accuracy than those extracted from the Envisat ASAR data because the PALSAR FBS (fine-beam single polarization) data has twice the resolution in the slant-range direction. PALSAR is also less affected by layover because of the incidence angle of ∼38° compared to the ∼23° incidence angle of Envisat IM beam 2 data, especially in the central Longmen Shan where many slopes exceed 30°. In addition, several of the Envisat pairs have long time intervals, which further degrades the crosscorrelation of the imagery. The range component of the pixel offsets from PALSAR is not significantly affected by ionospheric variations because the ionospheric phase propagation delays are on the order of the radar wavelength and a very small fraction of the radar range pixel size. Refraction in the ionosphere because of gradients in the along-track direction affects the azimuth offsets.

The along-track pixel offsets from the PALSAR FB data acquired in May and June 2008 are much less accurate than those from other PALSAR pairs, because they are heavily contaminated by large and sharp variations in the ionospheric total electron content (TEC) (Kobayashi *et al.* 2009; Raucoules & de Michele 2010). Sharp gradients in the TEC of the ionosphere can refract L-band radar propagation and result in along-track distortions of the imagery (Gray *et al.* 2000; Meyer & Nicoll 2008). Most of the PALSAR pairs have along-track offsets in roughly sinusoidal waves with northwest–southeast axes that are likely because of the ionosphere, as previously noted by Raucoules & de Michele (2010) and Kobayashi *et al.* (2009). Raucoules & de Michele (2010) also showed that it is possible to estimate the ionospheric TEC difference for a pair by integrating the azimuth offsets and then to mitigate the ionospheric delay of the InSAR measurements. The amplitudes of these waves reach up to 8 m of along-track offset, which is much larger than the 2–4 m of along-track displacements that are likely because of the earthquake. All of the PALSAR FB scenes were acquired on ascending satellite passes at roughly 22:30 local time, which is close to the time of maximum TEC instabilities resulting from night-time ion-electron recombination (Meyer *et al.* 2006). The PALSAR ScanSAR scenes were acquired at about 10:30 local time on a descending track, and the interferogram has no notable ionospheric effects, although it is not possible to extract pixel offsets because of the much coarser spatial resolution. All of the ascending PALSAR scenes acquired over this area during May and June 2008 show these effects of strong ionospheric waves with varying amplitudes and wavelengths but similar orientations. In our analysis, we did not attempt to remove the ionospheric effects by making empirical estimates of the ionospheric component and subtracting (Kobayashi *et al.* 2009; Raucoules & de Michele 2010), but we did limit the effects by only using the portions of the ascending PALSAR interferograms where the LOS motion was large compared to the ionospheric noise. We also use many other interferograms and GPS measurements so that the scenes with ionospheric effects have less influence on the slip inversions.

2.3 InSAR processing

InSAR pairs from the ALOS PALSAR stripmap or fine-beam data (Table 2) were formed and averaged by eight pixels in the crosstrack direction and 16 pixels in the along-track direction to produce interferograms with roughly 80 m dimensions on the ground, using ROI_pac (Fig. 2). PALSAR fine-beam dual polarization (FBD) scenes were oversampled to the FBS range sampling at the raw data step. InSAR pairs from the stripmap Envisat IM data were formed and averaged by 16 crosstrack and 80 along-track pixels to produce interferograms with approximately 320 m ground dimensions (Fig. 3). The poor coherence of the Envisat interferograms required more averaging. Topographic phase was calculated from the SRTM-CIATv4 DEMs and removed from the interferograms. The interferograms were smoothed with a power spectrum filter (Goldstein & Werner 1998) and then unwrapped with the SNAPHU program (Chen & Zebker 2002). Effective coherence after filtering was calculated and used with a threshold to mask out low

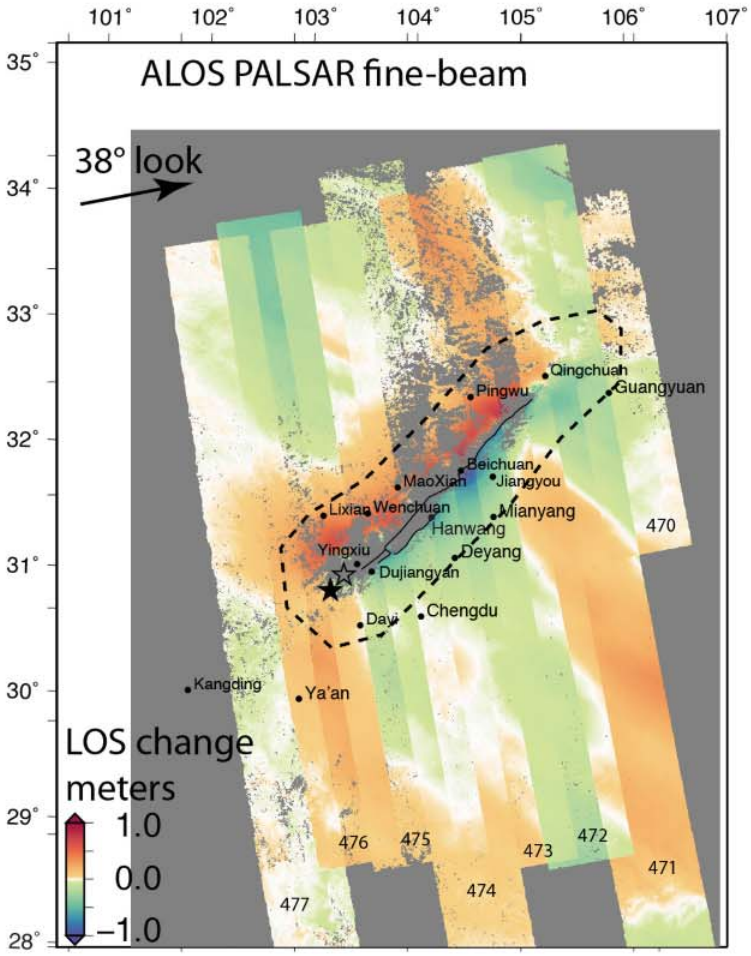

Figure 2. Mosaic of ALOS PALSAR fine-beam interferograms from the eight ascending tracks measuring LOS change measured from InSAR phase (track numbers at bottom of each scene). Wave-like features elongated in the northwest-southeast direction are likely because of ionospheric radar propagation delays. Black lines show surface ruptures, open black star shows USGS epicentre, and solid black star shows epicentre we used for slip evolution models. Positive LOS motion is away from satellite (i.e. east or down). Grey areas are where InSAR was incoherent so LOS motion could not be measured. Dashed polygon outlines area of large deformation used in slip inversions.

coherence areas and retain only the unwrapped phase in connected components likely to be reliably unwrapped. For PALSAR paths 473–475, the main fault rupture completely separates the northern and southern parts of the interferograms, so it was necessary to estimate the correct phase ambiguity of the northern side by comparing the interferogram phase of those paths to the adjacent paths in the overlap regions (Fig. 4). We assume phase ambiguities are resolved by this procedure and don't try to reestimate them in the modelling.

ScanSAR image acquisitions are more complicated than stripmap images because the SAR acquisition of each subswath is broken up into bursts rather than being continuous (Monti Guarnieri & Prati 1996). The bursts also have to overlap between the two images of an InSAR pair to give any coherence in a ScanSAR–ScanSAR interferogram (Monti Guarnieri & Prati 1996; Tong *et al.* 2010). Both Envisat WS and ALOS WB1 ScanSAR use five subswaths to image a wider swath, so that means the acquisitions spend less than 1/5 of the time imaging each subswath. The Envisat WS images were focused and interferograms formed with five cross-track and three along-track pixels averaged using the SARscape software, which uses the Monti Guarnieri & Prati (1996) technique. Because the coherence was very low on the two interferograms from tracks 204 and 247, we did not attempt further analysis. For track 476, the coherence was somewhat higher, but still low, so we performed additional averaging of four crosstrack by four along-track pixels to produce 320 m pixels before filtering and unwrapping with SNAPHU. The phase ambiguity of the northwest side of the fault ruptures relative to the southeast side was estimated by comparing to a preliminary model prediction.

The ALOS PALSAR WB1 pair from path 124 was processed using the Bamler & Eineder (1996) technique of adding zero pulses between the ScanSAR bursts, as described by Tong *et al.* (2010). This converts the ScanSAR data from each subswath into a faux stripmap data set that can then be processed with ROI_pac. We formed 10 interferograms (for the two frames with five subswaths each) and averaged 16 crosstrack and 64 along-track pixels (although the degraded along-track resolution of the ScanSAR data means that the effective number of along-track pixels averaged is probably closer to 10) to make products at roughly 240 m ground spacing (Fig. 5). Interferograms were filtered and unwrapped with SNAPHU. The relative phase difference between the subswath

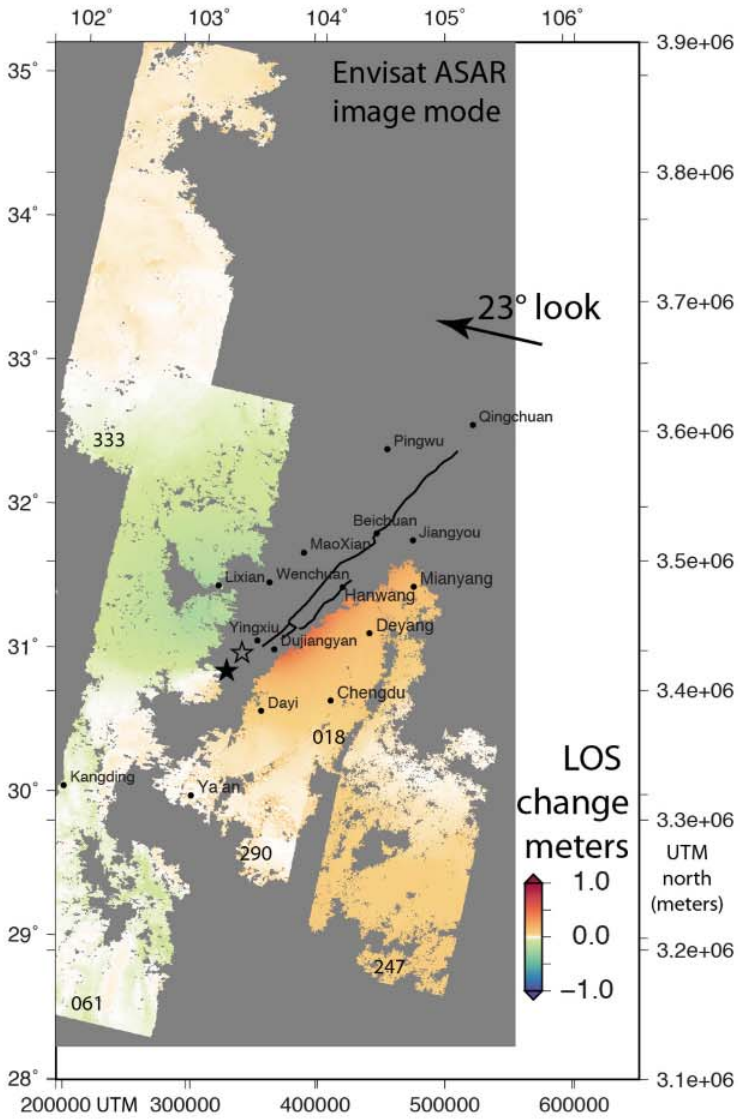

Figure 3. Mosaic of Envisat ASAR interferograms from five descending tracks in image mode (track numbers near bottom of each scene). This LOS is roughly opposite to the LOS of the ascending tracks, so positive motion is west or down. Shorter radar wavelength and longer time interval causes large areas to be incoherent on these interferograms (grey). Other annotations as in Fig. 2.

interferograms was estimated from the overlap areas, and the phase ambiguity across the fault was estimated by comparison to a preliminary model. For the PALSAR WB pair, the long spatial baseline, low resolution and incomplete overlap of the bursts cause low coherence in the areas of steep slopes.

2.4 Teleseismic data

We retrieved broad-band seismic records from the IRIS GSN. From the pool of stations available, we consider only teleseismic stations, located between 30° and 90° of azimuthal distance, to avoid triplication effects in the upper mantle and diffraction at the core–mantle boundary. Of this initial pool of available records, 21 *P*-wave and 14 *SH*-wave records were then selected to provide a good azimuthal coverage and maximize the resolution on the source (Fig. 6). For the azimuths with a great density of stations (Europe for instance), only records showing coherent and clear phases identified in most of the neighbouring records were retained. We only keep the first 140 s of the records, which contains the coherent part of the signal associated with the rupture process. Finally, the records are bandpass filtered using a Butterworth filter between 150 and 2 s period.

3 INVERSION FOR FINITE-FAULT SOURCE MODELS

3.1 Modelling strategy

We optimized the finite source slip models using the methods developed by Ji *et al.* (2002), which allow for joint inversion of seismic waveforms and coseismic static displacements measured by geodesy. There is substantial benefit in jointly inverting seismological and geodetic data, as shown in a number of previous studies

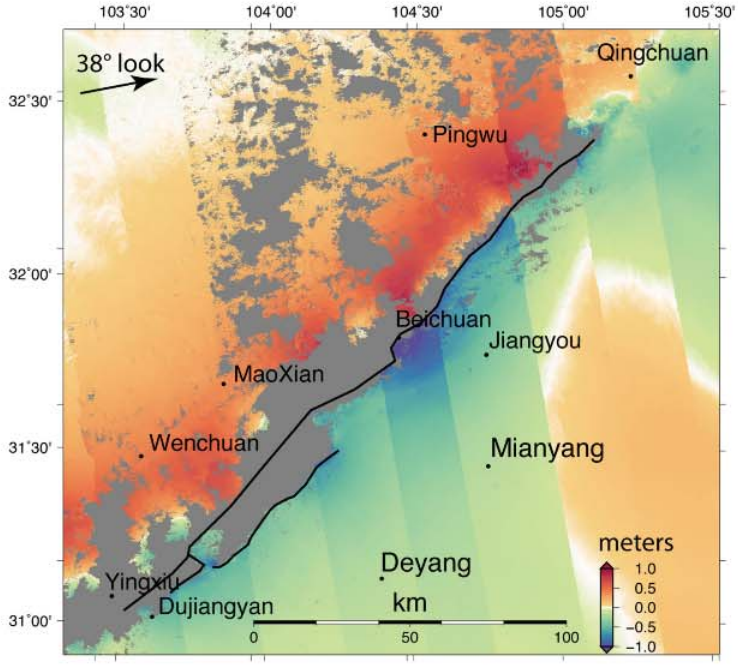

Figure 4. Enlargement of ALOS PALSAR fine-beam interferograms in area of main ruptures (same data as Fig. 2). Note that ground displacements in the ascending track radar LOS change sign close to much of the northwest side of the fault because the vertical motion towards the satellite is larger than the horizontal motion to the east away from satellite. Grey areas are incoherent parts of interferograms where ground motion was too large or disrupted to map, including many landslides.

(Hernandez *et al.* 1999; Delouis *et al.* 2000; Salichon *et al.* 2003; Hayes *et al.* 2010; Wei *et al.* 2011). The geodetic data from GPS and InSAR provide strong constraints on the spatial distribution of the total coseismic slip. Seismological data also provide constraints on the spatial slip distribution but is most sensitive temporal evolution of the earthquake ruptures, so the two data types are complementary. We first ran independent inversions of the teleseismic and geodetic data to examine the information provided by each data set and guide the selection of parameters for the final joint inversion models (Sladen *et al.* 2010).

Green's functions relate fault patch slip to deformation at the surface and to seismic wave generation. We compute the Green's functions for both the static and kinematic slip models using a layered elastic half-space with elastic constants derived from a local 1-D seismic velocity model (Table 3) extracted from the global 3-D CRUST2.0 model (Bassin *et al.* 2000). The seismic velocity and other elastic properties are constant in each layer. Because we are only analysing the teleseismic waveforms, the 1-D seismic velocity model is an adequate approximation despite the major variations in crustal structure across the Longmen Shan. Fault model segments are broken up into a set of patches or subfaults, with a size of 10 by 4 km. For both static and slip evolution models, we estimate the slip magnitude and rake of each patch. For the slip evolution models, we also estimate the rupture velocity that determines the onset and duration (commonly called rise time) of slip on each subfault. Our procedure requires an *a priori* choice of the hypocentral location, as the observed and predicted waveforms are shifted so that the onsets of the *P* waves match. This procedure means that the kinematic models are relatively insensitive to the errors of the predicted *P* wave traveltimes or the origin time. Optimization of the slip models is performed using a non-linear stochastic simulated annealing algorithm (Ji *et al.* 2002). We added regularization to the inversions by penalizing spatial roughness of the slip distribution measured by the spatial Laplacian, and the inversions all included a positivity constraint on the rake to enforce thrust and right-lateral slip. The factor controlling the degree of smoothing (weight of the roughness penalty) was chosen to balance the fit to the data against excessive oscillations in slip over short distances. The static slip inversions also have an additional penalty constraint on the difference between the final estimated moment and the moment of the Global CMT (Ji *et al.* 2002). The moment constraint helps to avoid the inversions adding large amounts of fault slip on deep fault patches that don't produce much surface deformation and therefore are not constrained by the geodetic data. This constraint also minimizes possible contamination of our coseismic model by the post-seismic deformation that is present in some of the data. It is also a way to take into account the broader constraints brought by seismology as the GCMT moment is based on a much larger data set of stations and on the radiated energy over a broader frequency range than our teleseismic data (we don't use the surface waves in our inversion). We checked our solution without moment constraint and find that the total seismic moment of the kinematic inversion ($M_0 = 9.5\text{e} + 20$ N.m, $M_w = 7.92$) is almost identical to the GCMT seismic moment imposed ($M_0 = 9.0\text{e} + 20$ N.m, $M_w = 7.90$).

3.2 Fault geometry

We used the surface ruptures that we mapped from the SAR pixel offset tracking to constrain the location of our modelled fault system at the surface (Fig. 7). Detailed field mapping of the coseismic ruptures (Liu-Zeng *et al.* 2009; Xu *et al.* 2009a) and the pixel offset data (see Fig. 7) (Kuo *et al.* 2008; Kobayashi *et al.* 2009; de Michele *et al.* 2010a) show that the fault ruptures at the surface are quite

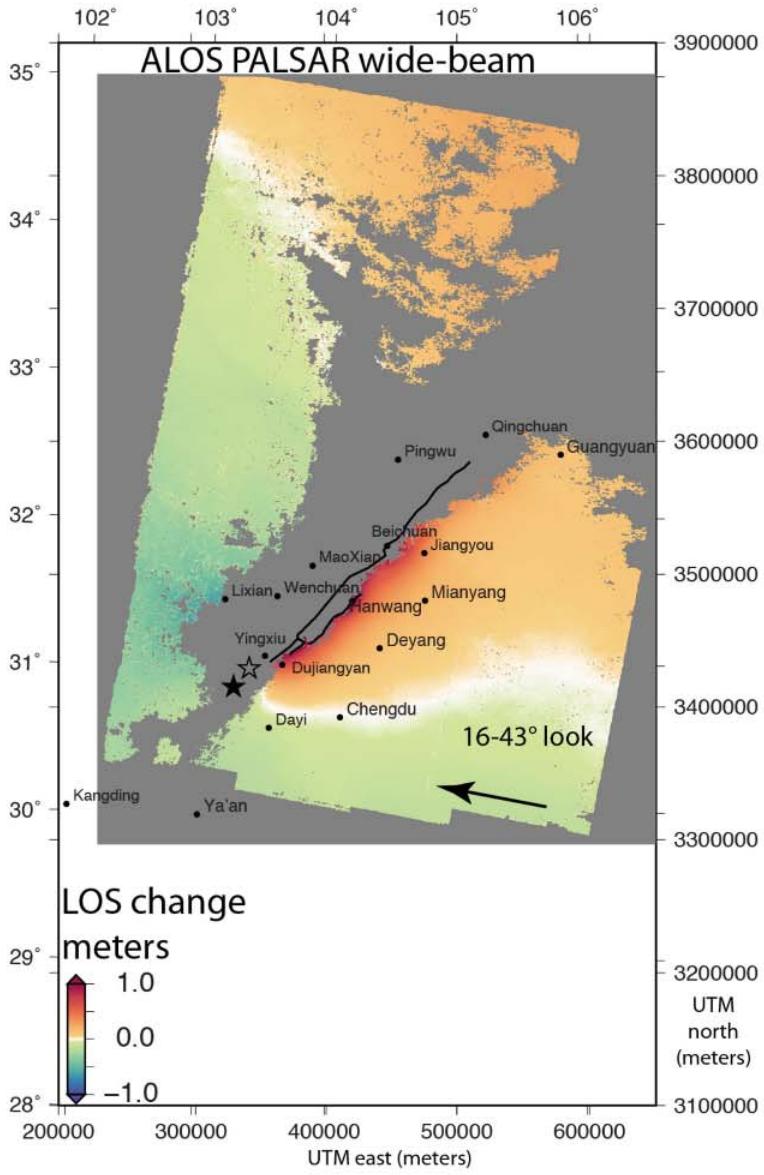

Figure 5. Wide-beam ALOS PALSAR interferogram from descending track. Five ScanSAR subswaths, with incidence angles varying from 16° on the east side to 43° on the west side, were combined, so LOS vectors change across scene. Positive displacements are west or down. Other annotations as in Fig. 2.

complex, with local variations in location and orientation of the faults in addition to rapid changes in amounts of coseismic slip. The two main faults that ruptured are the Beichuan Fault that runs along the front of the central Longmen Shan, and the Pengguan Fault (sometimes called the Guanxian-Anxian fault) that runs along a smaller range that is part of the fold and thrust belt in the Sichuan basin (Burchfiel *et al.* 2008; Hubbard & Shaw 2009; Xu *et al.* 2009a; Hubbard *et al.* 2010; Li *et al.* 2010), both with northeast strikes. There is also left-lateral slip of large magnitude (up to 2 m) on a short northwest-striking fault called the Xiaoyudong Fault (Fig. 7; Kuo *et al.* 2008; Liu-Zeng *et al.* 2009), which we do not attempt to model in this study. Because we are modelling the entire 280 km length of coseismic ruptures, we simplify the faults into a set of three segments for the Beichuan Fault (southern, central and northern) and two segments for the Pengguan Fault (shallow and deep), where each fault segment is planar (Fig. 8).

With the surface locations of the fault segments constrained, we then explored a number of different fault model geometries for the subsurface based both on structural geology studies (Densmore *et al.* 2007; Zhou *et al.* 2007; Burchfiel *et al.* 2008; Hubbard & Shaw 2009; Liu-Zeng *et al.* 2009; Xu *et al.* 2009a; Hubbard *et al.* 2010; Li *et al.* 2010) and on analysis of the pixel offset, InSAR and GPS data. The southern segment of the Beichuan Fault (≈50° dip) and the Pengguan Fault (≈30° dip) have parallel strike directions and the more steeply dipping Beichuan Fault is expected to converge with the more shallowly dipping Pengguan Fault at a depth around 20 km, depending on the dips (Fig. 8). Available seismic reflection profiles (Hubbard & Shaw 2009; Hubbard *et al.* 2010; Li *et al.*

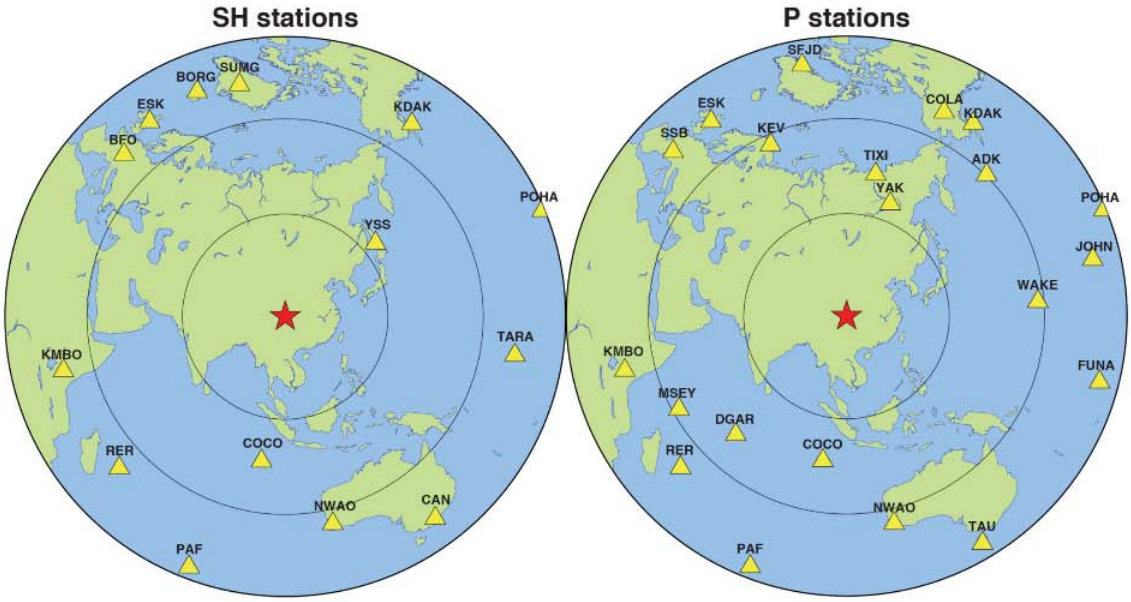

Figure 6. Distribution of teleseismic stations (yellow triangles) used in analysis: (left) *SH* waveforms, (right) *P* waveforms. Red star shows epicentre, equiangular projection. The black circles are placed every 30° of azimuthal distance. Letters show station ID codes.

Table 3. 1-D Velocity model used for the inversions.

Layer Thickness (km)	V_P (km s^{-1})	V_s (km s^{-1})	Density (g cm^{-3})
1	2.5	1.2	2.1
1	4	2.1	2.4
20	6.1	3.5	2.75
20	6.3	3.6	2.8
4	7.2	4.0	3.1
–[a]	8.0	4.5	3.4

[a]Thickness of bottom layer effectively infinite.

2010) image the Pengguan Fault and the other related faults in the Sichuan Basin, but don't extend into the steep mountains of the Pengguan Massif of the Longmen Shan to image the Beichuan Fault. In some studies, the faults beneath the Longmen Shan are modelled as curved listric faults with the dips decreasing at depth (e.g. Zhang *et al.* 2010). In the structural geology models derived from seismic reflection profiles of Hubbard & Shaw (2009), Li *et al.* (2010) and Hubbard *et al.* (2010), the Beichuan Fault and Pengguan Faults are splays off the same master fault with curved profiles. Because our model parametrization requires planar subfaults, we have simplified the fault geometry to keep the number of subfaults small without violating too much the geological constraints (Fig. 8). All the cells within a subfault are assumed to rupture according to the logical sequence determined by the rupture velocity and the location of where sliding starts (at the hypocentre for the first subfault and for the other segment according to the isochrons of the rupture on the neighbouring segments).

We made adjustments to the model fault geometry to better fit the InSAR and GPS observations in our static slip model inversions. In our preferred fault model (Fig. 8), we adopt a geometry that is similar to that of Shen *et al.* (2009), with the southern Beichuan fault (SBF) segment dipping at 45° to a depth of about 20 km, where it intersects, and presumably merges with, the more shallowly dipping deep detachment fault (DF) that we model with a fault segment dipping 5° to the northwest. This geometry is similar to that derived from seismic reflection profiles and other structural geology constraints (e.g. Li *et al.* 2010). We have a separate segment for the shallow Pengguan Fault (PF) dipping at 34° from the mapped surface ruptures down to 18 km depth to the northeast of the Xiaoyudong cross fault that appears to be located at a major NW-trending structural discontinuity. The modelled central Beichuan Fault (CBF) and northern Beichuan Fault (NBF) segments extend to a depth of 25 km, with dips of 55° and 70°, respectively.

3.3 Inversion data selection

For the finite fault slip inversions, we used the geodetic measurements from Wang *et al.* (2011) in our finite source inversions. This data set includes 468 campaign GPS sites and represents a significant improvement over the 158 GPS sites previously available (Shen *et al.* 2009). During our fault model optimizations, we found it impossible to fit the motions of one GPS station, H050, which is near the epicentre, and still fit the other GPS and InSAR data, so we left that station out of the final inversions. We removed two levelling points and three additional GPS stations (ROHS, YBSH and YTSH) that are too close to the fault trace to be compatible with our fault geometry and its discretization (subfaults are 10 km × 4 km). We also removed the vertical component of several GPS points (W041, W056, W172, W173, W177 and SD07), which had anomalously high amplitudes compared to the values at surrounding stations.

We used down-sampled InSAR range change measurements from the eight ALOS PALSAR stripmap interferograms on the ascending paths, the ALOS PALSAR ScanSAR interferogram on the descending path, the four Envisat ASAR stripmap interferograms (descending tracks), and the Envisat ASAR descending track 476 ScanSAR interferogram. Down-sampling is necessary to reduce the millions of data points in the interferograms to less than a thousand samples for each interferogram (see Fig. S1). The down-sampling was optimized for imaging the slip on the main Beichuan fault using the Lohman & Simons (2005) method, which results in more samples close to the fault and fewer samples at greater distances, with

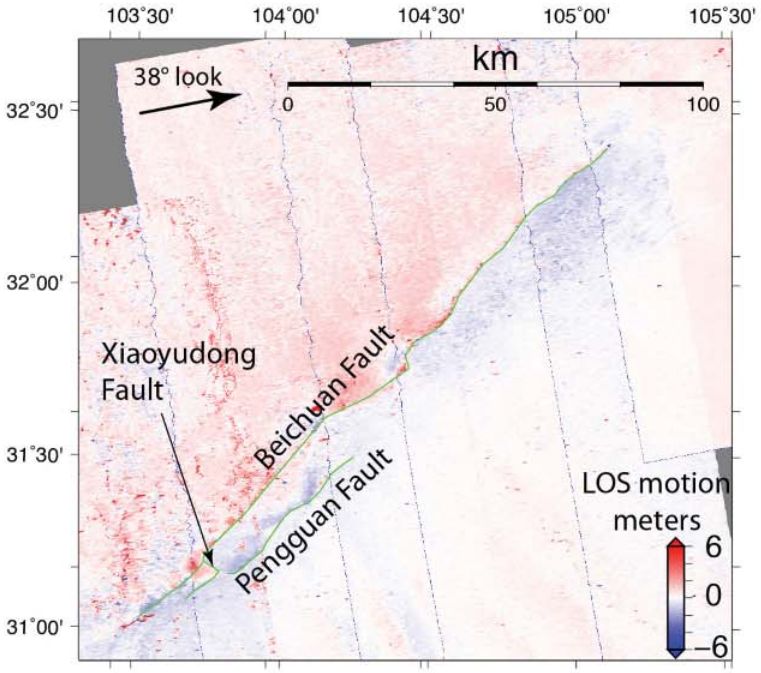

Figure 7. Surface displacements in the radar line of sight (LOS) from subpixel correlation of ALOS PALSAR fine-beam images. Green lines show surface ruptures mapped from discontinuities in these LOS offsets and other subpixel correlation measurements from ALOS and Envisat SAR. Positive displacement is away from the satellite and indicates motion towards the east or downward.

InSAR data averaged in squares around each down-sampled point. We use a variable LOS vector for all the interferogram samples. The ALOS PALSAR FB swaths have LOS vectors inclined between 36° and 41° from the local vertical (also called the incidence angle). The PALSAR WB swath LOS varies from 17° to 44° from the vertical, similar to the Envisat WS mode LOS that varies from 16° to 45° from the vertical. The Envisat IM beam 2 swath has incidence angles between 19° and 27° from the vertical.

As mentioned above, all of the PALSAR FB ascending path 470–477 scenes acquired in May and June 2008 after the Wenchuan earthquake are contaminated with effects from waves in the ionospheric TEC to various degrees. The variations in the ionosphere not only affect the along-track pixel offsets, but also the InSAR phase measurements (Gray *et al.* 2000; Meyer *et al.* 2006; Raucoules & de Michele 2010). On two of the PALSAR FB interferograms, from paths 470 and 476, the peak-to-peak apparent variations of range change caused by the ionospheric waves reach about 1 m over a 200 km distance. To mitigate the errors because of these atmospheric effects, we use only the portions of the PALSAR interferograms within about 50 km of the surface ruptures for the inversions (see dashed line on Fig. 2), because this is where the deformation signal is large compared to the ionospheric noise. We used the full path 477 interferogram, which has much smaller ionospheric effects. The daytime descending PALSAR WB and all the Envisat interferograms show no clear sign of ionospheric effects, but will have some effects from tropospheric water vapour. We find that the tropospheric water vapour measured by the NASA Moderate Resolution Imaging Spectroradiometer (MODIS) and ESA Medium-resolution Spectrometer (MERIS) instruments can reach up to 6–7 cm of total precipitable water vapour in the Sichuan Basin, which could cause as much as 40 cm of radar propagation delay and apparent range change, but we have not attempted to correct for these effects in this study. The interferograms will only include the difference in water vapour delay between the two acquisition dates. Because MERIS and MODIS only measure total column water vapour in cloud-free areas, they also don't provide complete measurements over the perpetually cloudy Longmen Shan.

3.4 Static slip inversion

We first performed inversions for the static slip during the earthquake using the InSAR and GPS data. The static slip inversions only estimate the total slip on each patch of the modelled faults, not the temporal evolution of slip, reducing by two the number of free parameters per fault patch. Hence, they are much more rapid and stable to compute than slip history model optimizations. As described in Section 3.2, we explored a variety of subsurface fault geometries for the fault segments to determine a geometry that is consistent with the geodetic data for the coseismic deformation.

The InSAR and GPS data near the northeast segment of the Beichuan fault (NBF) require that slip on this segment be nearly pure strike-slip and that the fault dip be steep, because the deformation decreases rapidly with distance to the northwest of the surface trace. We also found that to match the geodetic data, especially PALSAR path 470 and the GPS data, we needed to extend the fault segment about 50 km to the northeast from the end of the surface ruptures mapped in the field and by the SAR pixel offsets (see Fig. 8). In our final preferred model, the dip of this segment is 70°, but other steep dips give similar results. The central segment of the Beichuan fault (CBF) starts just southwest of the city of Beichuan, where there is a sharp bend in the surface ruptures that we approximate as an offset between fault segments in our simplified models. We use a dip of 55° for the CBF in our preferred model, consistent with the geological observations of the fault ruptures at the surface

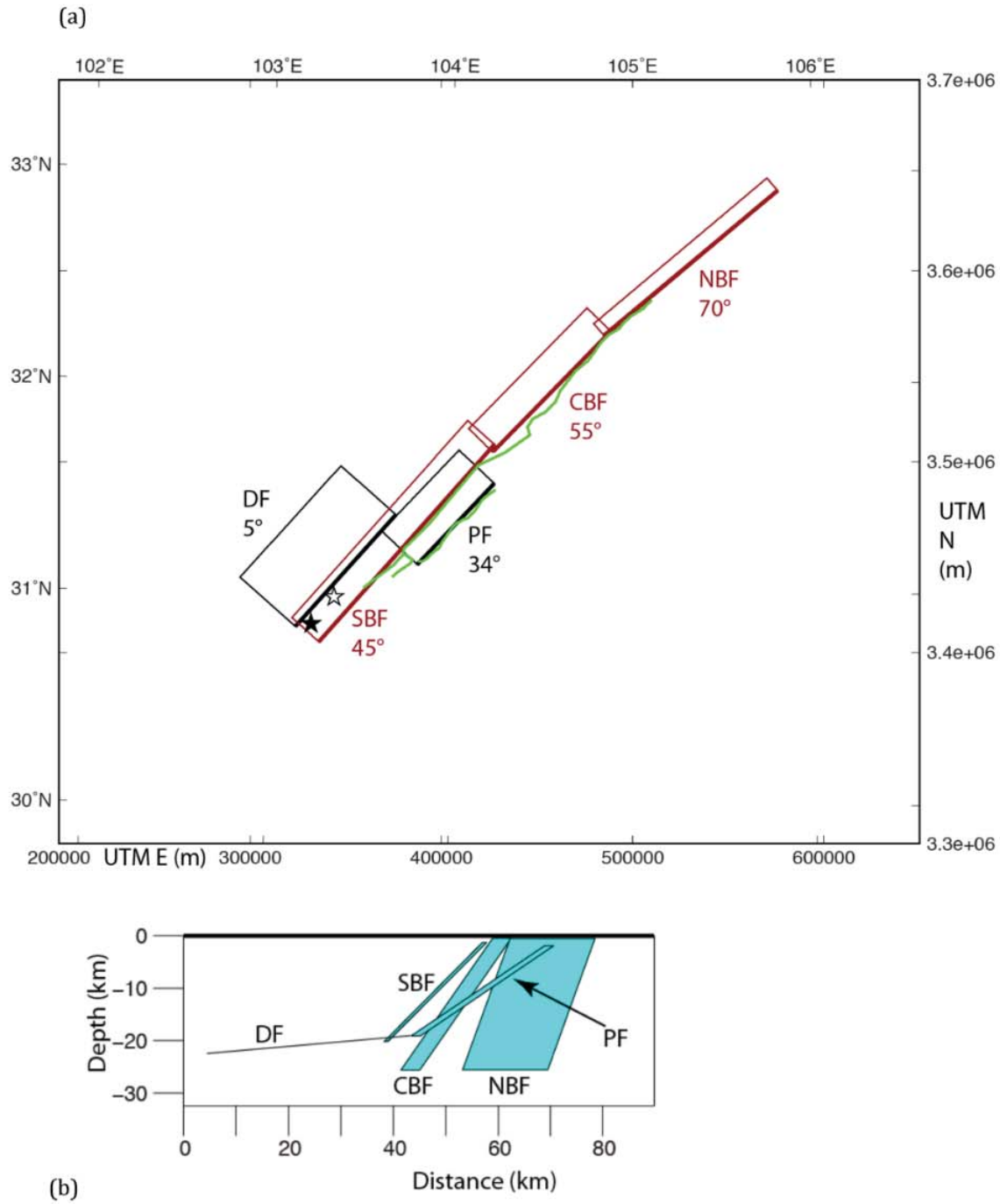

Figure 8. (a) Map view of our preferred fault geometry model, simplified into five rectangular fault segments. Red lines are outlines of three segments of Beichuan Fault: south (SBF), central (CBF) and north (NBF). Black lines are outlines of Pengguan Fault (PF) and deep detachment fault (DF) segments. Thicker lines mark top edges of fault segments and dip of each segment is labelled. (b) Horizontal view of fault segments looking along the strike of the southern Beichuan Fault (SBF), azimuth 41°. Central and northern Beichuan Fault segments (CBF and NBF) are oblique to this view so their true dip is not shown.

(Liu-Zeng *et al.* 2009) and optimal dips determined from geodetic data in other studies (Shen *et al.* 2009).

The InSAR and GPS data require that there be significant slip far to the northwest of the surface trace of the southwestern end of the Beichuan Fault because the horizontal motions towards the fault extend far in that direction. However, because the displacements don't provide strong constraints on the depth of this slip, our model deep detachment fault (DF) dip of 5° is essentially the

same as the horizontal dips of Shen *et al.* (2009) and Wang *et al.* (2011).

We tested different amounts of smoothing (varying the weighting of the spatial roughness penalty function) and selected the largest smoothing factor that still allowed a good fit to the geodetic data. In the joint inversions, we adjusted the smoothing factor to approach a comparable roughness in the slip model results, although the joint inversion preferred solution is somewhat rougher than the other solutions because of the larger number of parameters and observations involved. In our preferred geodetic-only solution (Figs 9, 10b and 11a), the total length of the rupture reaches about 280 km, although slip decreases rapidly past 250 km from the hypocentre. This is similar to what was inferred by previous static (e.g. Shen *et al.* 2009; Wang *et al.* 2011) or back-projection studies (e.g. Xu *et al.* 2009b; Zhang & Ge 2010). The slip distribution reaches a maximum slip amplitude of 16 m about 50 km northeast of the epicentre and is characterized by along-strike rotation of the rake angle, which changes from pure-thrust motion near to the epicentre to almost strike-slip motion towards the northeastern end of the rupture (Fig. 11a). With a few exceptions for GPS points near the surface rupture, the fit to both the GPS and InSAR data is excellent (Figs 10 and S3) in both the near and far field. Despite the levelling measurements and surface fault offsets not being used in the inversion, our slip model is also able to fit these data very accurately (Fig. 9).

There is a systematic underprediction of the vertical displacements of GPS stations on the footwall near Beichuan (see Fig. 10b). This is partly because of our simplified fault geometry for the central segment of the Beichuan Fault, which is up to 10 km away from the actual fault location at the surface in this area where the fault has large deviations. Our model fault may not match the likely changes in dip with depth either. The underprediction also could be caused by our simplified layered elastic structure that does not include the much softer material of the Sichuan Basin sedimentary rocks. Another possibility is a subsurface extension of the Pengguan Fault or related blind thrusts further north as proposed by de Michele *et al.* (2010a). Finally, almost all of the GPS stations in that area were measured in campaign mode, so the errors on the vertical displacements are relatively high. Monument instability or local compaction could also be a factor in some cases.

To evaluate the resolution of our inversions of the geodetic data, we performed a checkerboard test keeping the same parametrization as for the other inversions (geometry, range of values for the slip parameters, velocity model, etc.). We forward calculated synthetic InSAR and GPS observations with the same spatial distribution as the actual data samples and stations from a checkerboard slip model with 3 × 3 subfault (30 × 12 km) patches of 10 m slip alternating with patches of zero slip (see Fig. S2a). Comparison of the input checkerboard slip model pattern (Fig. S2a) and the slip model obtained from the inversion of the synthetic data (Fig. S2b) indicates that most of the slip distribution, at the scale of the 30 × 12 km pattern, can be recovered, both in shape and in slip amplitude. The inversion fits most of the synthetic GPS observations very well (Fig. S2c). As expected, we note a decrease in resolution for the deepest subfaults of the Beichuan Fault, especially for the central and northern segments that have steeper dip angles. On the other hand, the slip pattern of the deep Pengguan fault segment, deep but with a shallow dip, is recovered with little smearing (limited to a distance of one cell). Overall, this resolution test demonstrates that the slip distribution can be well resolved, as expected from the very large amount of geodetic data sets. The inclusion of teleseismic data in our joint inversions should somewhat improve the resolution of deep slip on the faults.

3.5 Teleseismic-only slip inversions

We ran kinematic slip model inversions using only the teleseismic data. A very early inversion implementing a single fault with its strike (229°) and dip (33°) taken from the GCMT solution provided a look at the earthquake before geodetic data were available (http://www.tectonics.caltech.edu/slip_history/2008_e_sichuan/e_sichuan.html). We started with the epicentre location estimated from the global body-wave solution from the USGS NEIC. With our preferred fault geometry, this horizontal location falls onto the southern Beichuan Fault (SBF) segment, and would require the depth of the hypocenter to be at about 10 km, considerably shallower than the NEIC estimated hypocentral depth of 20 km. Because of the large lateral variations in lithospheric velocity structure across the Longmen Shan and the eastern edge of Tibet, earthquake horizontal locations and depths estimated from both teleseismic and regional networks depend strongly on the details of the velocity models used (Sun *et al.* 2004), so a horizontal or depth location error for the hypocentre would not be surprising (Engdahl *et al.* 1998). For the joint slip inversions, we estimated a shifted hypocentre location as discussed below in Section 3.6.

Our preliminary teleseismic-only results showed a unilateral northeast-propagating rupture with the rake rotating from near thrust to strike-slip over a length of about 250 km [http://www.tectonics.caltech.edu/slip_history/2008_e_sichuan/e_sichuan.html (last accessed 30 April 2013)], similar to other teleseismic-only inversions (Ji & Hayes 2008, available from http://earthquake.usgs.gov/earthquakes/eqinthenews/2008/us2008ryan/finite_fault.php). The source models discussed in this study use the same multiple fault segment geometry as the static-only inversions. Realistic fault geometry is indeed critical to help reconcile the teleseismic model with the geodetic data (Konca *et al.* 2010).The teleseismic-only inversions with the full five-subfault geometry were helpful to optimize the bounds on the rupture velocities. They also helped to estimate the time delays between the initiations of ruptures on the five fault segments of the preferred model. We find that rupture propagation velocities around 2–2.5 km s^{-1} fit the teleseismic data well. The teleseismic models all show a rather bumpy source time function with a total duration of about 100 s and a gradual change of the source mechanism from a dominantly thrust rupture to a dominantly right-lateral strike-slip rupture as the rupture propagates northeastwards. The teleseismic source models are consistent to first order with the geodetic data in terms of the length of the rupture and along-strike variations of the type of faulting (Fig. 11b). However, because of the numerous trade-offs among the model parameters, the seismic-only models do not match well the near-field geodetic data (Figs S4 and S5). This is simply because seismology constrains rather well the timing and shape of the moment release (relative to the origin time) and the pattern of radiated energy, but only poorly constrains the spatial distribution of moment release, especially if only teleseismic data are used. Including local or regional waveforms from strong motion or high-rate GPS stations can provide strong constraints on slip evolution models (e.g. Wei *et al.* 2012), but this also requires detailed information about 3-D velocity structure and fault geometry.

3.6 Joint kinematic slip inversions

Kinematic slip models from joint inversion of geodetic and teleseismic data combine the spatial constraints on the final slip distribution with the temporal constraints. Seismic waveforms represent a

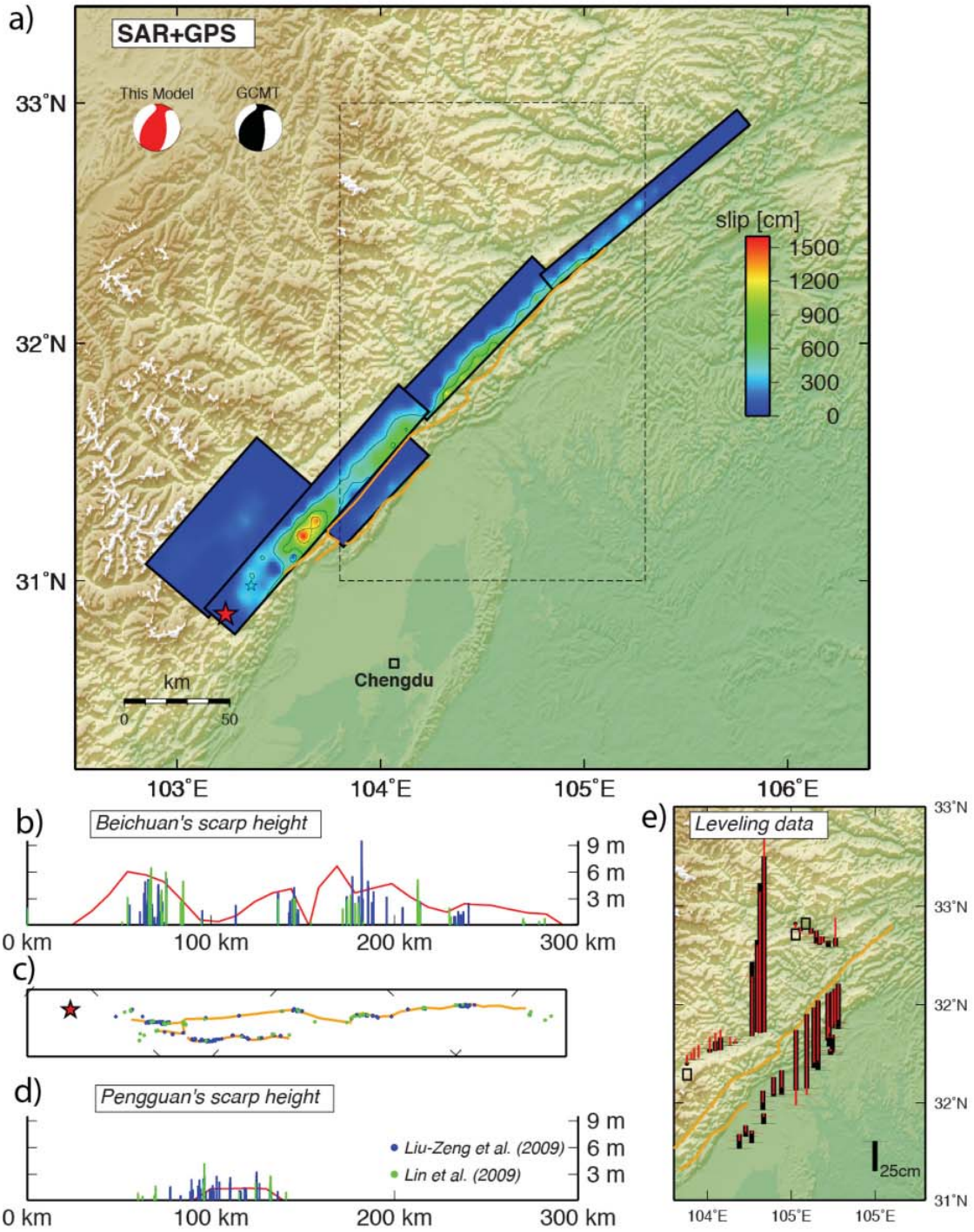

Figure 9. (a) Map view of slip distribution from geodetic-only slip model superimposed on a topographic map. Dashed outline box shows area plotted in (e). (b) Profile along Beichuan Fault showing offsets measured in the field (green) (Lin *et al.* 2009) and (blue) (Liu-Zeng *et al.* 2009). Red line shows total slip in the top 10 by 4 km patch of preferred model. (c) Map view of field surface rupture measurement locations (green and blue dots) on rupture lines mapped from SAR subpixel correlation (orange lines). (d) Profile of field offset measurements along Pengguan Fault with same symbols as (b). (e) Levelling profile measurements and model predictions on detailed map of central area. Red bars show vertical displacements from levelling profiles (Wang *et al.* 2009), and black bars show our model predictions.

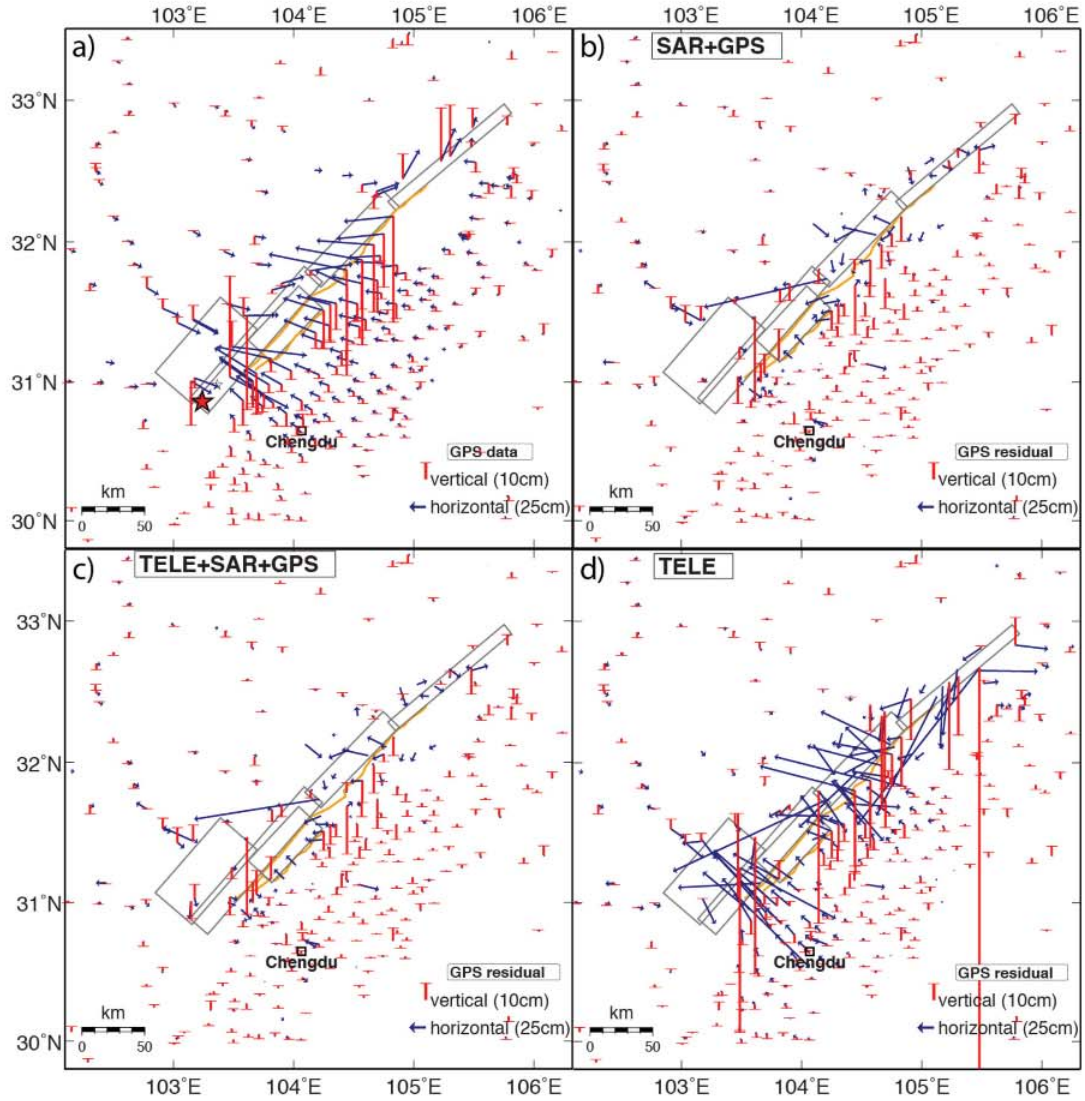

Figure 10. GPS observations and residuals from model fits. Blue arrows are horizontal displacements and red lines with bars are vertical displacements. (a) GPS coseismic displacements with 95 per cent error ellipses on horizontal vectors, which are mostly not visible at this scale (Wang *et al.* 2011). (b) Post-fit residuals from our geodetic-only model (static inversion of InSAR and GPS data). (c) Post-fit residuals from our preferred kinematic slip model from joint inversion of geodetic and seismic waveform data. (d) Residuals from predicted surface deformation of our teleseismic waveform inversion.

spatial integration of the radiated wavefield, implying that the spatial variations can only be detected through small time shifts related to the directivity effect. Hence, the results of the geodetic-only inversion can be used to narrow down rupture velocity by checking the correspondence between the slip peaks of the geodetic-only slip model and the timing of the high-amplitude arrivals seen in the teleseismic *P* waveforms. To avoid time-shifts related to the directivity effect, we choose four teleseismic stations with azimuths roughly perpendicular to the fault to compare the spatial distribution of slip from the geodetic data inversion with the timing of slip from the teleseismic inversion. The obtained time–distance plot (Fig. 12) shows that, on average, the rupture velocity didn't vary strongly and remained in the 2.5–3 km s^{-1} range. Indeed, we tested different rupture velocities (we always allow for small rupture velocity variations of ± 0.2 km s^{-1}) for our joint inversion model and found that a rupture velocity of 2.8 ± 0.2 km s^{-1} allows the inversion to best fit the amplitude of the *P* waveforms. To do those tests we had to define the location of the epicentre. We find the USGS epicentre location (30.986°N, 103.364°E) to be too close to the first high-slip patch to be compatible with a rupture velocity of about 2.8 ± 0.2 km s^{-1}. This means that either the rupture started slowly (below 2 km s^{-1}), as suggested by a recent study with empirical Green's functions (Wen *et al.* 2012), or that there is some error in the USGS epicentre location. Because teleseismic epicentres in this area have significant uncertainty, for our kinematic inversion we use a hypocentre location shifted roughly 10 km to the southwest (30.914°N, 103.348°E) and assume a fairly constant rupture speed of 2.8 km s^{-1} all along the fault. The depth of the hypocentre is adjusted to match the depth of the southern Beichuan Fault (SBF) at that location (10 km). Early up-dip rupture and

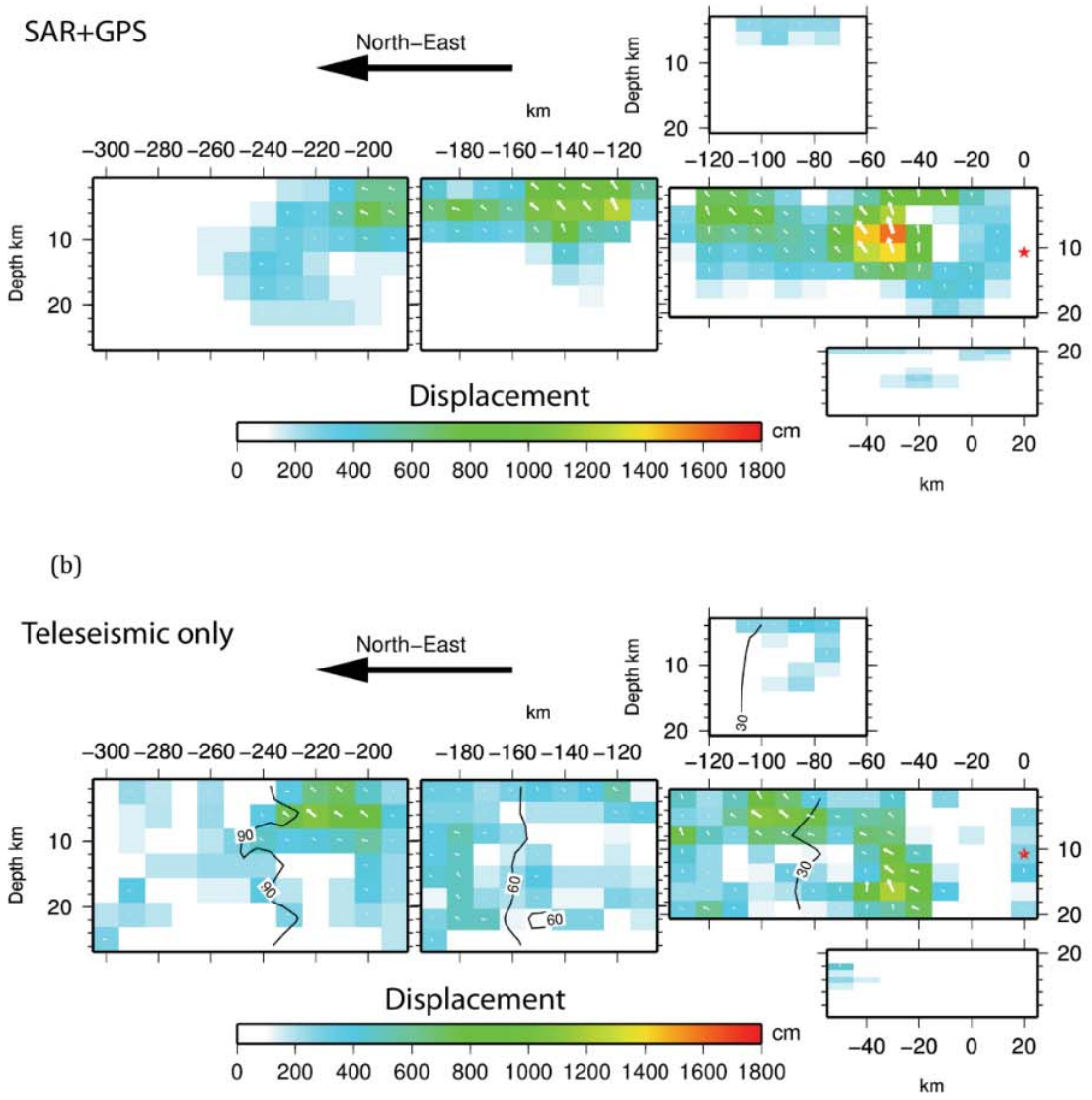

Figure 11. Slip distributions from finite fault models. Along-strike distance in km from hypocentre is shown in horizontal direction, depth in km is shown in vertical direction. For better visualization, the deep detachment fault has been plotted with a 15° dip instead of its actual 5° dip in our fault model. (a) Displacements on each fault segment of static model from inversion of geodetic data only. Colours show magnitude of slip on each fault patch, white arrows show rake or slip direction. Red star shows location of the hypocentre. (b) Final displacements on each fault segment of kinematic model from inversion of teleseismic data only. Contour lines show timing of rupture in seconds. (c) Final displacements on each fault patch of kinematic model from joint inversion of teleseismic, SAR and GPS data. Black contour lines show time (seconds) from start of earthquake that fault slip began on each patch. (d) Rise time or duration of fault slip on each fault patch of kinematic slip evolution model from joint inversion.

along-strike propagation are difficult to distinguish from teleseismic waveforms, so our estimated model hypocentre location has large uncertainty.

The implementation of the kinematic slip modelling with multiple fault segments that we use (Ji *et al.* 2002) also requires the specification of the linkage between the fault segments to determine how the rupture propagates. We link the bottom of the southern Beichuan fault (SBF) segment to the deep detachment fault (DF) segment where they intersect so that the rupture front propagates downwards from the Beichuan fault in our preferred model. The rupture then propagates to the northeast along the central and northern Beichuan Fault (CBF and NBF) segments linked at their ends, and upward along the shallow Pengguan Fault (PF) segment, linked at its bottom to the deep detachment fault (Fig. 8). All of these segment links have zero time delay. The kinematic inversion with these linkages has a total rupture time of 110 s to reach the northeast end of the faults (Fig. 11c).

Our joint inversion slip model fits the GPS observations almost as well as the geodetic-only inversion with very similar residuals (Figs 10b and d). It also fits the InSAR observations with similar residuals (Fig. 13). This is because the geodetic data strongly controls the spatial distribution of slip, even in the joint inversion. Fits to the seismic waveforms are also very good, at least for the first 90 s (Fig. 14).

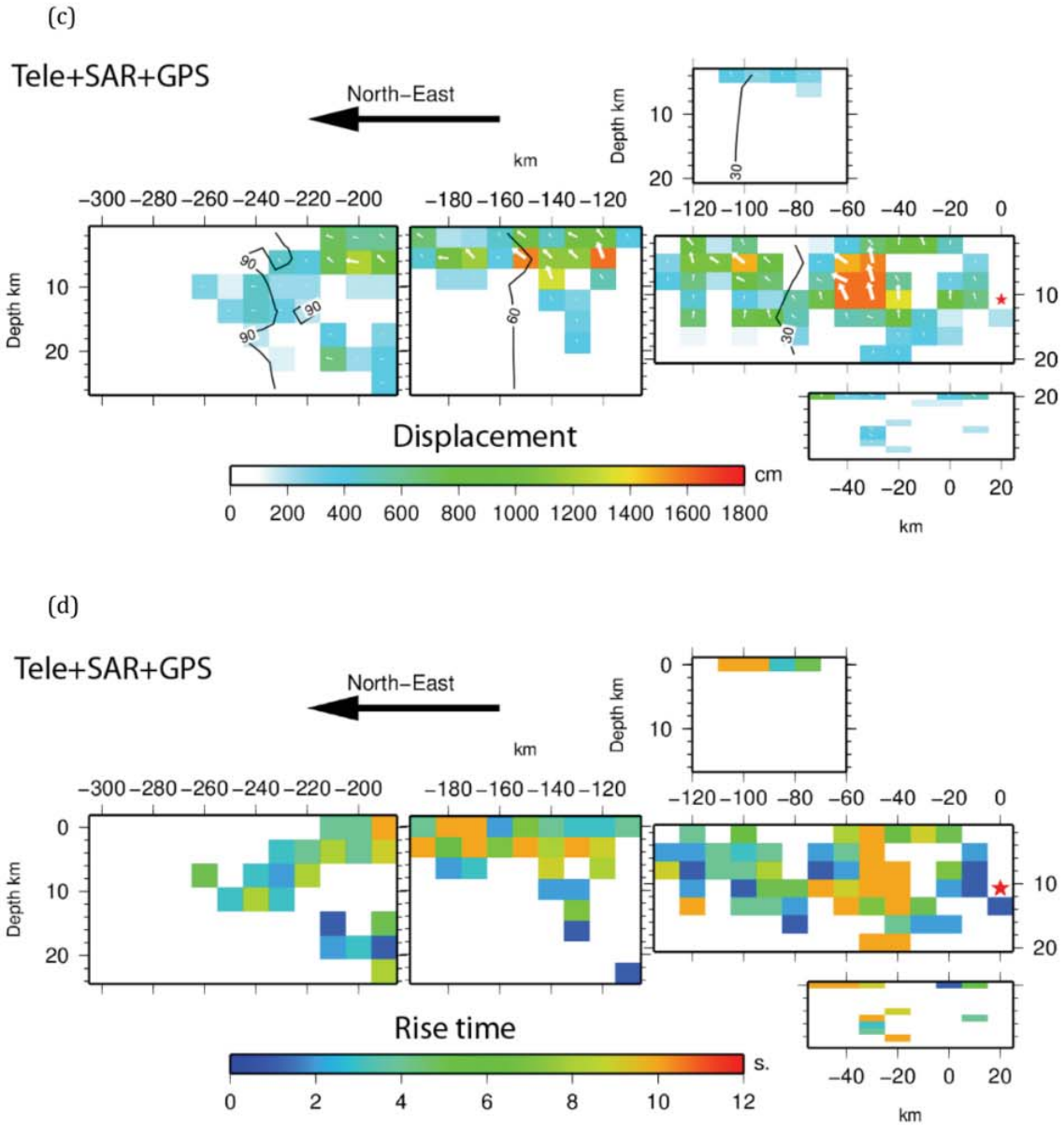

Figure 11. (*Continued.*)

The slip distribution of our preferred model (Figs 11c and 15) can be mainly described by four areas of high slip: in the southwest part of the Beichuan fault (SBF), we obtain two patches of respectively 16 and 10 m peak slip amplitude, which roughly coincide with the ends of the parallel Pengguan fault trace at distances of about 50 and 100 km from the hypocentre (Fig. 11c). The third patch of high slip, which has a maximum slip of 13 m, is located near the town of Beichuan about 120–150 km from the hypocentre on the CBF segment, just north of the main offset of the Beichuan fault between our SBF and CBF segments. In our preferred joint inversion (Figs 11c and 16), this slip peak is divided into two peaks about 30 km apart, but the static solution has only one broad peak (Fig. 11a), so the geodetic data only requires one peak in slip at this location. Finally, the rupture ends with a patch of moderate amplitude with a peak slip (maximum 8 m) about 200 km from the hypocentre and then gradually decreasing slip for a total rupture length of about 280 km. For the most part, the Wenchuan earthquake is a shallow rupture with most of its slip limited to the upper 14 km of the crust, except at the southwestern end.

At the southwestern end of the part of the Beichuan Fault that ruptured in 2008, InSAR and GPS data indicate that fault slip extends farther away from the Beichuan Fault, in the northwest direction, as shown by the 20 cm of displacement measured by GPS stations more than 100 km from the Beichuan Fault (Fig. 10). To match that signal, the inversion requires a patch of larger slip amplitude (16 m) on the SBF and extending deeper (18 km) than the average on the Beichuan fault, but it also requires some relatively small amplitude slip (a few metres) on the subhorizontal deep detachment fault (DF).

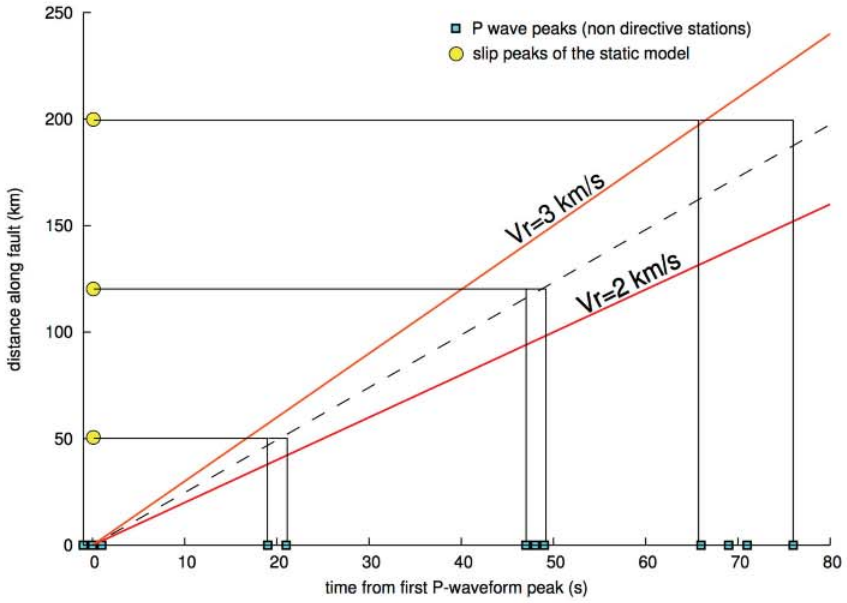

Figure 12. Plot of horizontal along-strike location of areas of large slip in the static slip model (vertical axis) compared to the time of large peaks in the amplitude of *P* waves observed at non-directive stations (horizontal axis). The correspondence of the spatial and temporal peaks gives an estimate of the average rupture velocity between high-slip patches.

Our distribution of final slip on the Beichuan fault is similar to static models that used similar sets of data and fault geometry (e.g. Shen *et al.* 2009; Wang *et al.* 2011). The main difference is that our slip model has peak slip values in the subfaults between 4–8 km instead of near the surface. This might be because of the less effective spatial smoothing in the joint inversion because of the larger number of parameters (slip evolution) than the geodetic-only inversion.

The deep subhorizontal detachment fault was included in the static slip models of some previous studies (Shen *et al.* 2009; Wang *et al.* 2011), but the distribution of slip on it is probably not well determined given the depth of that fault (about 20 km in our model and the others) and the fact that the geometry is poorly constrained. In addition, neither our model, nor the other published fault slip models (Shen *et al.* 2009; Wang *et al.* 2011), includes lateral variations of the elastic structure or 3-D seismic velocity variations, which are expected between Tibet and the Sichuan Basin (e.g. Zhang *et al.* 2009). The relatively small amount of slip is not detectable in the teleseismic waveforms. However, the presence of slip on the décollement is supported by the aftershock relocation studies, which show increased activity towards the NW for that specific section of the fault (e.g. Li *et al.* 2010). Thus, the presence of the deep subhorizontal slip patch doesn't seem to be a bias related to the nearby NW–SE profile of GPS measurement points. We note, however, that the slip on the deep fault could be post-seismic, because all of the GPS and InSAR measurements include days to months after the main shock.

As expected from our parametrization of the problem, our preferred kinematic slip model, obtained from the joint inversion of the teleseismic, GPS and InSAR data, has a slip distribution (Figs 11c and 16) very similar to the geodetic-only model (Figs 9 and 11a), with a maximum slip amplitude of 16 m and a rotation of the rake angle from thrust to strike-slip motion as the rupture propagates (Fig. 11c). The model is also characterized by a rather bumpy source time function that lasts about 110 s (Fig. 16a) and rise times around 10 s for the high-slip patches (Fig. 11d). The total seismic moment of the model is 9.5 e + 20 N.m, equivalent to $M_w = 7.92$. This is similar to the GCMT estimate (9.0 e + 20 N.m), and our preferred geodetic-only solution (9.25 e + 20 N.m) when using the same elastic structure model.

4 DISCUSSION

4.1 Overall characteristics of the source of the Wenchuan earthquake

In this study we have been able to produce a source model of the M_w 7.9 Wenchuan earthquake that is constrained by an exceptionally large set of SAR and GPS data. These data place important constraints on the fault geometry and the spatial distribution of slip. In addition, the combination with the seismological data allows estimation of the kinematic slip evolution during the rupture. The earthquake initiated at the southwestern extremity of the rupture and propagated unilaterally along the Beichuan Fault to the northeast, over a distance of about 280 km at an average rupture velocity of about 2.8 km s^{-1}. This result is consistent with the results from the back projection of high-frequency signals (e.g. Xu *et al.* 2009b; Zhang & Ge 2010). Rise times are found to be of the order of 10 s for the fault patches with large slip (Fig. 11d), although there is a trade-off between local variations of rupture velocity and rise time. Although the rupture velocity found in this study is in the usual range of rupture velocity estimated for large dip-slip earthquakes, the rise times inferred here are quite long in comparison to other large continental thrust events. In this regard, it is instructive to compare the Wenchuan earthquake to the M_w 7.6 1999 Chi-chi earthquake and the M_w 7.6 2005 Kashmir earthquake. These two events are also large intracontinental thrust earthquakes, for which relatively well-constrained source models could be derived from the joint inversion of geodetic and seismological data using the same technique as this study (Ji *et al.* 2001; Avouac

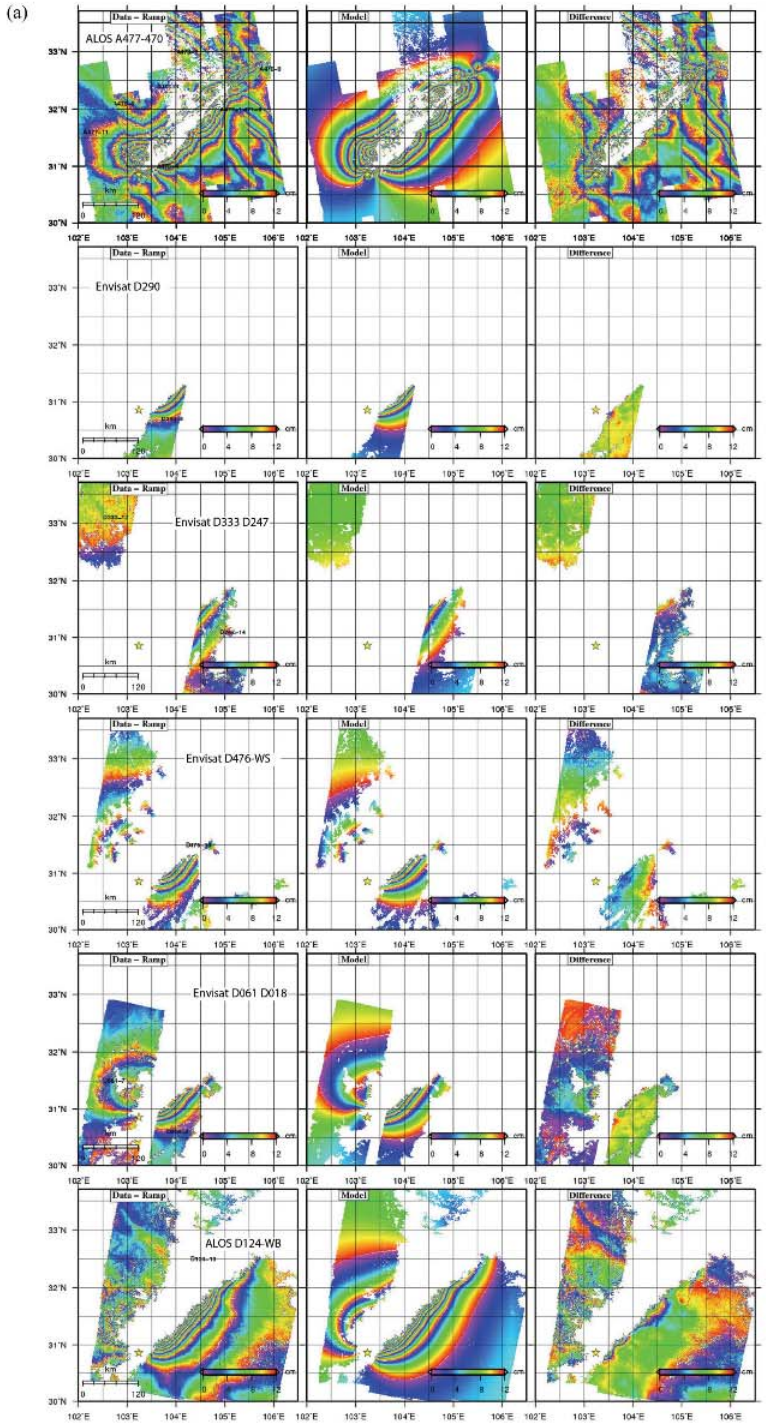

Figure 13. Maps of InSAR data after ramp removal (left column), preferred kinematic model final slip prediction from joint inversion projected into radar LOS (centre) and difference between data and model (right). (a) Wrapped interferograms, where the LOS motion has been rewrapped with a 12 cm colour cycle. Interferogram tracks are listed in each row. (b) Unwrapped interferograms where the colour scale is continuous with a range between −80 and 80 cm.

et al. 2006). Both of these events were significantly smaller than the Wenchuan earthquake, with rupture lengths of the order of 80 km and durations of about 30 s and moments about 3–4 times smaller (2.7×10^{20} Nm for Chi-chi earthquake and 2.9 10^{20} N.m for the Kashmir earthquake). The Chi-chi and Kashmir earthquakes both had rupture velocities of about 2.0 km s^{-1}, lower than our estimate for Wenchuan, and comparable rise times to Wenchuan although somewhat smaller for the Kashmir earthquake (5–7 s for Chi-chi,

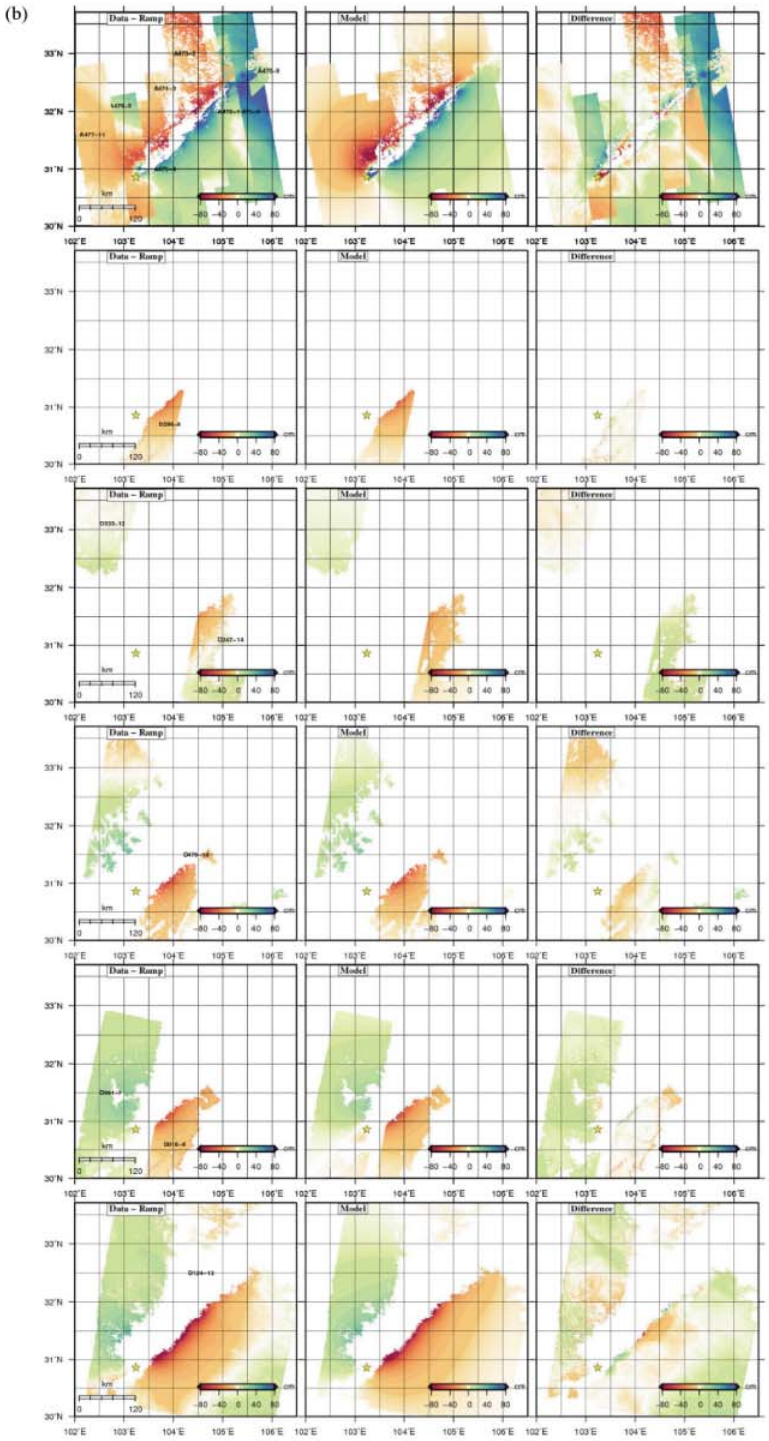

Figure 13. (*Continued.*)

2–5 s for Kashmir). Comparison of the source time functions show comparable peak moment rates, but the source time function of the Wenchuan earthquake is very irregular, suggesting a cascade of subevents.

The notion that the Wenchuan earthquake is a compound event is consistent with the highly segmented and contorted surface ruptures. In agreement with field mapping (Liu-Zeng *et al.* 2009; Xu *et al.* 2009a), the SAR data indeed revealed a complicated rupture

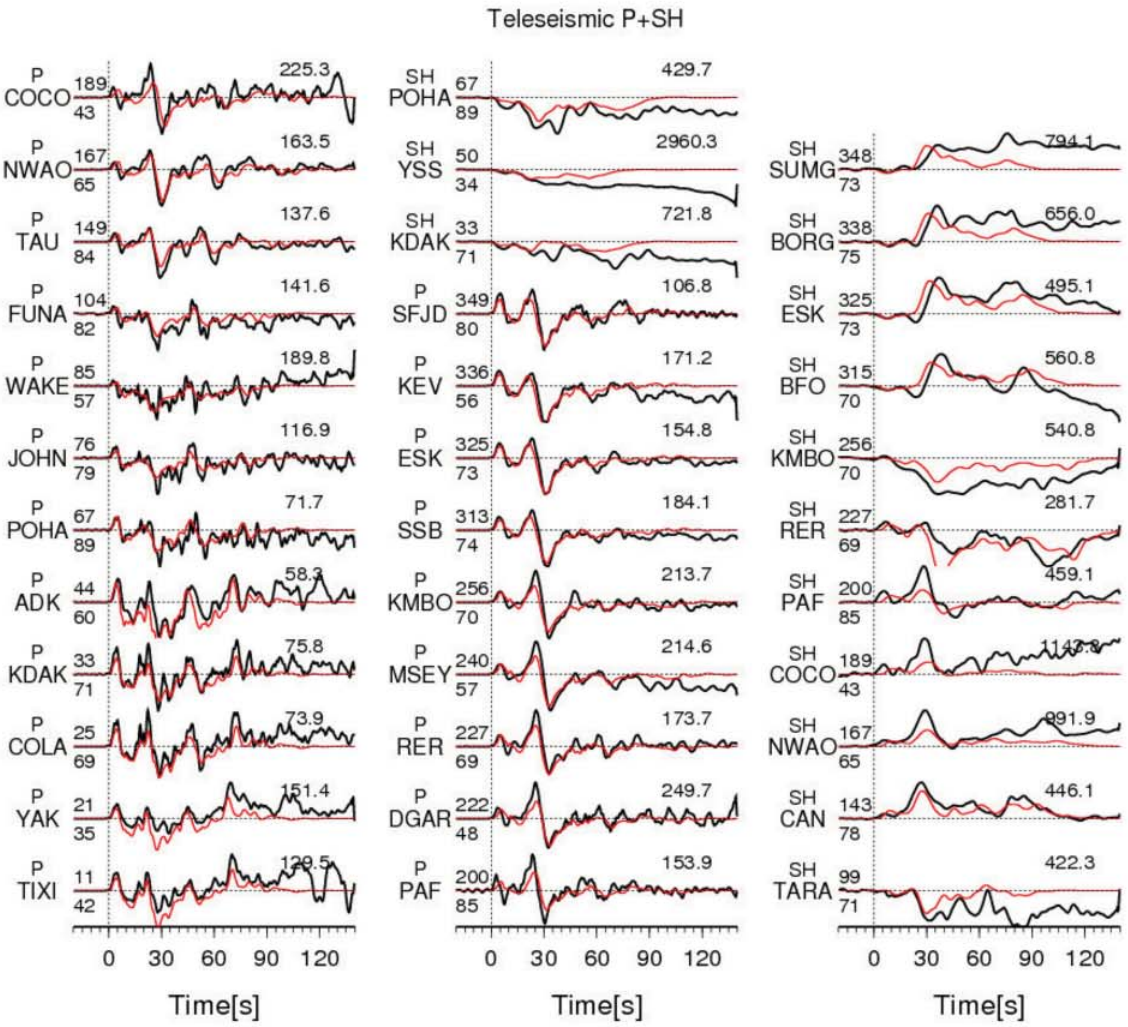

Figure 14. Fits to teleseismic waveforms by preferred kinematic slip evolution model from joint inversion. Black lines are observed and red lines synthetic seismograms.

with quite significant changes of strike of the main rupture and secondary faults at nearly 90° from the mean strike, including the Xiaoyudong fault and the lateral ramp south of Beichuan (Fig. 7). It is not uncommon to see ruptures ending at such geometric complexities (Segall & Pollard 1980; Sibson 1985; Manighetti *et al.* 2005; Wesnousky 2006) but less frequent to see a single earthquake rupturing through such apparently strong complexities (e.g. Shen *et al.* 2009; Wei *et al.* 2011). Some complexities in the surface ruptures may be shallow features not present in the faults at depth. Another noteworthy and unusual aspect of the Wenchuan earthquake is that it simultaneously ruptured two parallel fault strands lying about 20 km apart, the southern Beichuan Fault (SBF) and the shallow Pengguan Fault segment (SBF), over a distance of nearly 50 km. Parallel surface ruptures have been observed in cases of slip-partitioning, when one fault strand is purely dip-slip and the other is purely strike-slip (e.g. Klinger *et al.* 2005). The southern Beichuan Fault (SBF) segment, the Pengguan Fault (PF), and the deep detachment fault (DF) segments all have primarily thrust motion, but the central Beichuan Fault has some strike-slip motion (and the northern Beichuan Fault is almost pure strike-slip), indicating incomplete slip partitioning (Liu-Zeng *et al.* 2009). The near-simultaneous rupture of two subparallel fault splays with similar sense of motion has been previously considered unusual, although another example was imaged by InSAR in central Tibet where two subparallel normal faults ruptured a week apart (Ryder *et al.* 2010). Our analysis is unable to resolve the timing of the relatively small slip on the Pengguan Fault because we only use teleseismic waveforms.

4.2 The Wenchuan earthquake in the context of Longmen Shan tectonics

Several models have been proposed to explain the abruptness of the edge of the plateau formed by the Longmen Shan. One mechanism is eastward flow in the lower crust of Tibet that is limited by the old and cold crust of the Sichuan block, resulting in crustal thickening and uplift of eastern Tibet with a sharp edge and little shortening of the upper crust (Royden *et al.* 1997; Kirby *et al.* 2000; Burchfiel

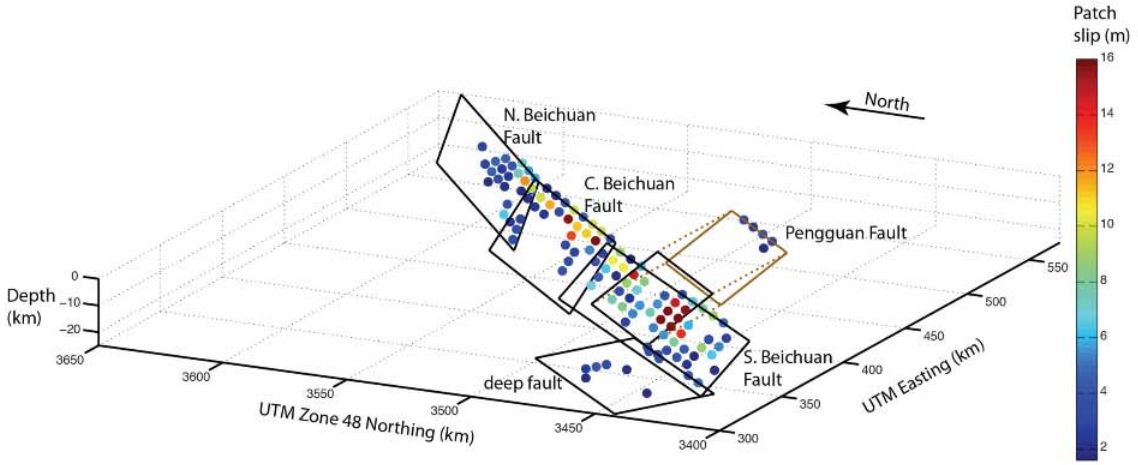

Figure 15. Three-dimensional perspective view of fault and total slip of preferred kinematic slip evolution model viewed from the southwest. Patches with slip of less than 1.5 m are not plotted. Colours show the magnitude of the final slip on each fault patch drawn as a circle for simplicity, even though patches are actually 10 by 4 km rectangles. To better visualize the Pengguan Fault (PF), the fault patches are plotted in a shifted location (brown rectangle). Dashed brown lines show connection to actual location of the PF.

et al. 2008; Royden *et al.* 2008). Another model involves large-scale thrusting of the Tibetan crust over the edge of the Sichuan block and partial reactivation of the Mesozoic fold-thrust belt in the Sichuan basin (Hubbard & Shaw 2009; Hubbard *et al.* 2010; Liu-Zeng *et al.* 2011). Recent analysis of lithospheric flexure from gravity data indicates that the Longmen Shan is flexurally supported by the Sichuan Basin lithosphere (Fielding & McKenzie 2012), which is consistent with substantial overthrusting. Finally it has also been proposed that the Longmen Shan owes its steep topography to the fact that its core basement is made of granitoids and metamorphic rocks exhumed from mid-crustal depth, much more resistant to erosion than the surrounding sedimentary lithologies (Godard *et al.* 2010). The significant slip on the detachment fault at midcrustal depth and the large slip on the Beichuan Fault in our preferred model is consistent with thrusting of at least the upper crust of Tibet over the edge of the Sichuan Basin.

The combination of thrust slip on the Beichuan and Pengguan Faults in our model causes uplift >1 m over a substantial area of the Longmen Shan (see Figs 17 and S6a). The greatest uplift is in the area of the Pengguan Massif that is the steepest mountain front of the Longmen Shan (Kirby *et al.* 2008; Hubbard & Shaw 2009; Li *et al.* 2010). The zone of significant coseismic uplift is much narrower than the zone of significant horizontal deformation (Figs 17a–c and S6b–c), as is expected for faults that are steep near the surface. In the central Longmen Shan (southwestern portion of the 2008 ruptures), the uplift extends about 50 km to the northwest of the Beichuan Fault. The uplift coincides with the steep slope of the mountain front and the area of greatest relief at the 40 km scale of the swath profiles (Figs 17a and b). This is also the area identified as the zone of active differential rock uplift based on the longitudinal profiles of rivers (Kirby *et al.* 2003) and the pattern of erosion rates derived from river incision rates and cosmogenic dating and river sands (Godard *et al.* 2010).

In the central Longmen Shan, the southeastward horizontal coseismic displacements (shortening) extend a long distance to the northwest from the Beichuan Fault as measured by InSAR and GPS (Figs 2–6, 9a and 17a). The shallowly dipping deep detachment fault (DF) in our model has significant slip to match this deformation. The model prediction is 1 m of fault-perpendicular displacement at 40 km and 0.5 m at 70 km from the Beichuan Fault on the Yingxiu profile (Fig. 17a). The geodetic data constrain the horizontal location of this deep fault slip, but not its vertical location, so we can't resolve the difference between a listric fault geometry with a horizontal deep detachment fault at a depth of ~20 km (Shen *et al.* 2009) and the shallowly dipping fault in our model. The important point is that the slip on the deep thrust fault must extend about 50 km to the northwest of the Beichuan fault, well into the high elevation part of the Longmen Shan and perhaps beneath eastern Tibet (Fig. 17).

The northern Longmen Shan has a much less steep mountain front than the central and southern part of the range (Figs 1 and 17). As many authors have noted, the steep topographic front makes a turn to the north at longitude ~104°E, forming the Min Shan (Kirby *et al.* 2000; Kirby *et al.* 2003), with the Longmen Shan to the east having moderate relief (Fig. 1). The devastated city of Beichuan is on the northeast side of the transition zone. The Min Shan (eastern margin of the Tibetan Plateau, north of the Sichuan Basin) was the site of two large M7.2 earthquakes in 1976 (Jones *et al.* 1984) and appears to have rapid rock uplift according to geomorphic and surface age dating (Kirby *et al.* 2000). The junction between the southern and central Beichuan fault segments in our model is close to the change in the Longmen Shan topography. Our preferred slip model has primarily thrust slip on the southern Beichuan, Pengguan, and deep detachment faults (SBF, PF and DF), intermediate oblique slip in the central Beichuan fault, and nearly pure strike-slip motion on the northern segment. This means that the amount of uplift on the NW side of the rupture varies in the same way as the topographic relief across the mountain front at the location of the fault.

Seismic reflection profiles and other structural geology data show that the thrust fault equivalent to the Beichuan Fault in the northeastern part of the Longmen Shan has a shallow dip and may sole into a detachment at 7–10 km depth (Xu *et al.* 2009a; Li *et al.* 2010). The GPS and InSAR data, however, show that the coseismic displacement was on a steeply dipping strike-slip fault extending to 20 km depth. This indicates that the 2008 rupture was not on the thrust fault previously identified as the northern Beichuan Fault (Xu *et al.* 2009a; Li *et al.* 2010). The fault that the main shock ruptured is actually about 40 km to the NW of the mountain front in

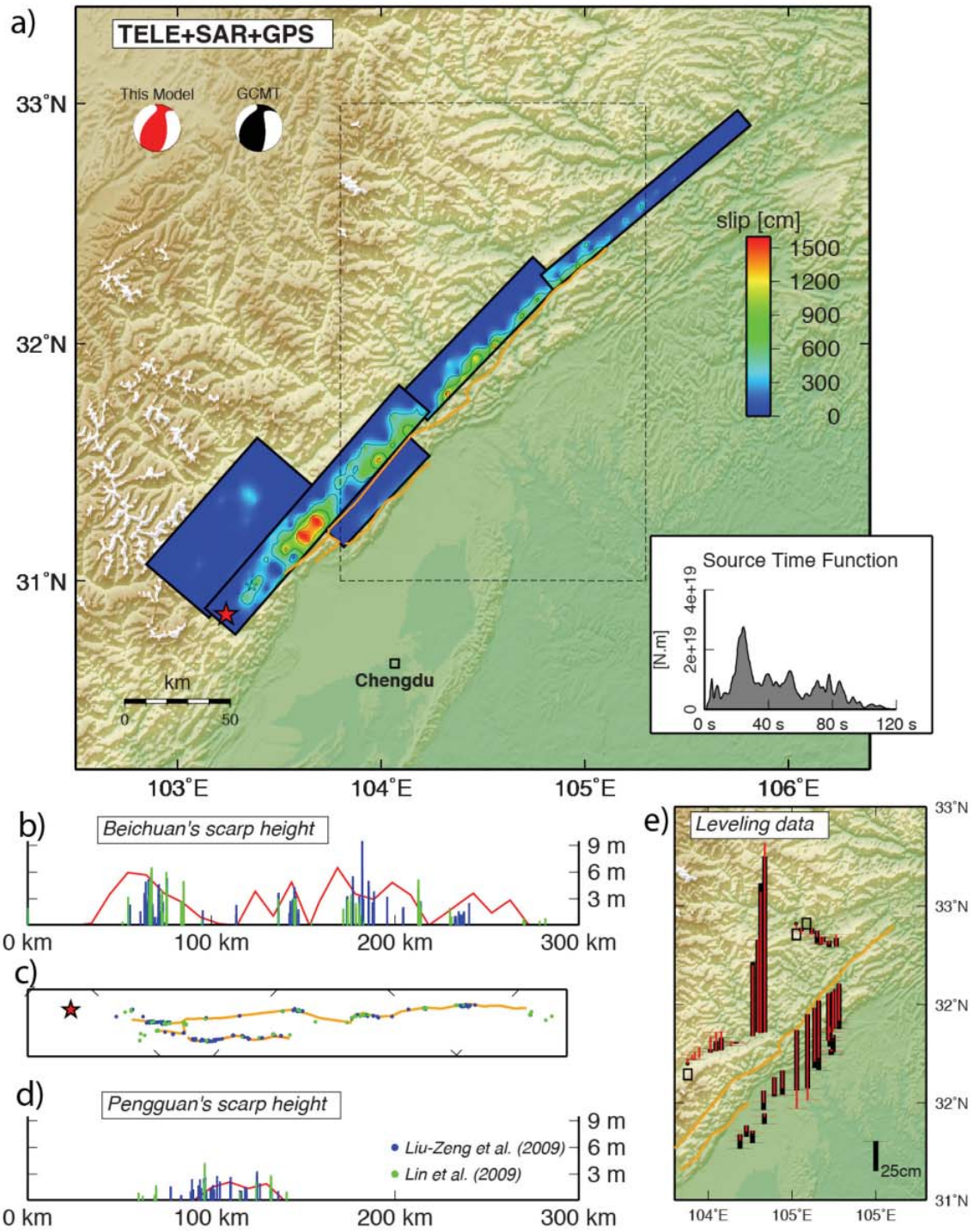

Figure 16. (a) Map view of slip distribution of our preferred kinematic slip model from joint inversion of teleseismic, InSAR and GPS data superimposed on a topographic map. Dashed outline box shows area plotted in (e). (b) Profile along Beichuan Fault showing offsets measured in the field (green) (Lin *et al.* 2009) and (blue) (Liu-Zeng *et al.* 2009). Red line shows total slip in the top 4 × 4 km patch of preferred model. (c) Map view of field surface rupture measurement locations (green and blue dots) on rupture lines mapped from SAR subpixel correlation (orange lines). (d) Profile of field offset measurements along Pengguan Fault with same symbols as (b). (e) Levelling profile measurements and model predictions on detail map of central area. Red bars show vertical displacements from levelling profiles (Wang *et al.* 2009), and black bars show our model predictions.

the northeastern profile between Pingwu and Qingchuan (Fig. 17d), so it is inboard of part of the system of thrust faults that forms the Longmen Shan there. We have been calling it the northern Beichuan Fault (NBF), but it might be better described as a part of the steeply dipping strike-slip Qingchuan Fault system, although the main Qingchuan Fault is located further north (Xu *et al.* 2009a).

It is interesting to note the similarity between the pattern of uplift predicted from our co-seismic model with the morphology of the mountain front, in particular its along-strike variations. Also we note that our coseismic model predicts very little subsidence of the foreland (Fig. 17), where there is an absence of a well-developed Cenozoic foreland basin. There is no doubt that long-term rates of convergence between the Longmen Shan and the Sichuan Basin are small; interseismic GPS rates are 4 mm yr^{-1} or less (Shen *et al.* 2009) and difficult to resolve with the available measurements before the 2008 earthquake. Based on the contrasts of erosion rates across the Pengguan and Beichuan faults, Godard *et al.* (2010) estimate the slip rate on the single thrust fault on which they both root (equivalent to the DF in our fault model), to be between 0.5 and 0.8 mm yr^{-1}. Such a rate would be consistent with the geodetic data and require the return period of earthquakes similar to the Wenchuan earthquakes to be very long, of the order of 6000 to 10000 yr (assuming an average slip of 5 m). The absence of a well-developed foreland basin could be explained by the small co-seismic subsidence we observe, allied with the fact that because of the little space made available for deposition, and easy bypassing, the sediments shed from the range are for the large part transported away to the South China sea. So the basic relationship between the topography and tectonic activity would not be that different from that observed along the more active Himalayan edge of Tibet, which is also consistent with the gravity signal of flexural support of the Longmen Shan (Fielding & McKenzie 2012). The high flexural rigidity of the Sichuan Basin lithosphere also helps to reduce the depth of the foreland basin near the mountain front. In addition, there is a large wedge of Mesozoic sedimentary rocks that fill in the western Sichuan Basin and hide the downward flexure of the lithosphere during both the Mesozoic and Cenozoic overthrusting (Jiang & Jin 2005; Hubbard *et al.* 2010; Fielding & McKenzie 2012).

The thrust-slip rupture of the Beichuan Fault at the base of the topographic front of the central Longmen Shan is somewhat similar to the rupture of the 2005 Kashmir earthquake that occurred at the topographic front of the northwestern Himalaya (Avouac *et al.* 2006; Pathier *et al.* 2006), although the structure of that part of the Himalaya is complicated by the nearby syntaxis and large Kashmir Basin. The major difference for the Wenchuan earthquake would be because of the exhumation of rocks highly resistant to erosion at a small distance from the range front (Godard *et al.* 2010). In

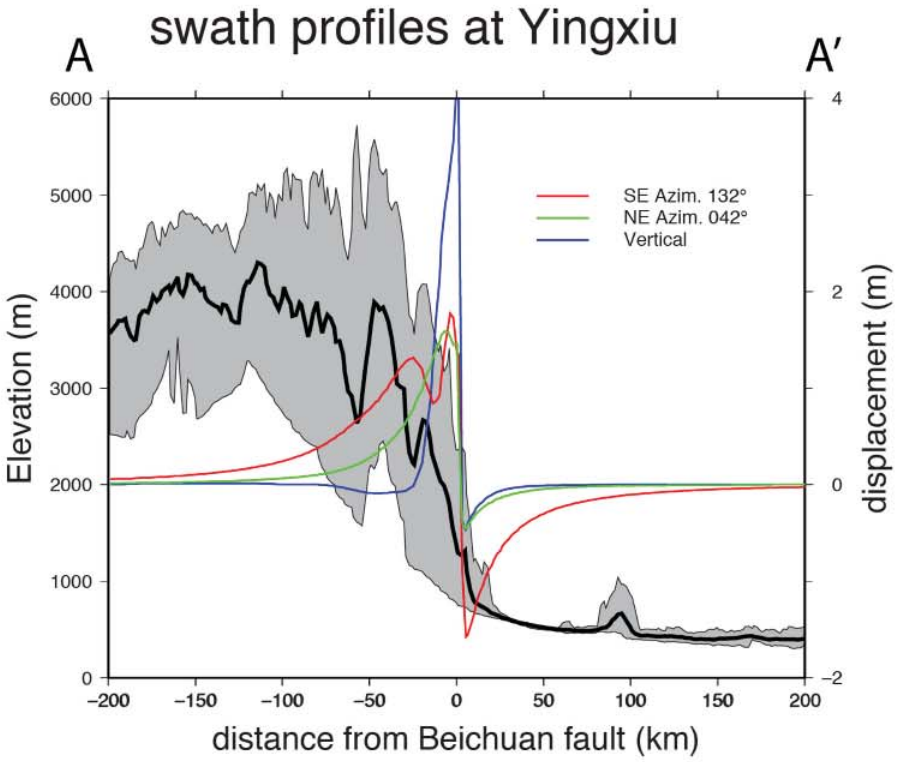

Figure 17. Swath profiles of topography, predicted displacement from preferred model and observed displacements from GPS and levelling across Longmen Shan mountain front. Locations of profiles shown on Fig. 1(a). Mean topography in bins 40 km wide (normal to profile) and 5 km along profile shown as thick black line with scale to left. Area between maximum and minimum elevations (thin lines) within bins is filled with grey. Model predictions are plotted as solid coloured lines separated into components: vertical (blue), normal to fault (red), and fault-parallel (green) with scale to right. (a) Profile A-A′ near city of Yingxiu close to epicentre of earthquake in southern Longmen Shan. (b) Profile B-B′ through town of Hanwang crossing Pengguan Fault (Hanwang segment) and Beichuan Fault at edge of Pengguan Massif in central Longmen Shan. (c) Profile C-C′ through city of Beichuan at edge of transition to northern Longmen Shan. Vertical displacements from levelling (Wang *et al.* 2009) plotted with open circles and from GPS (Wang *et al.* 2011) plotted with plus marks. (d) Profile D-D' through point between Pingwu and Qingchuan near northeast end of surface ruptures in northern Longmen Shan.

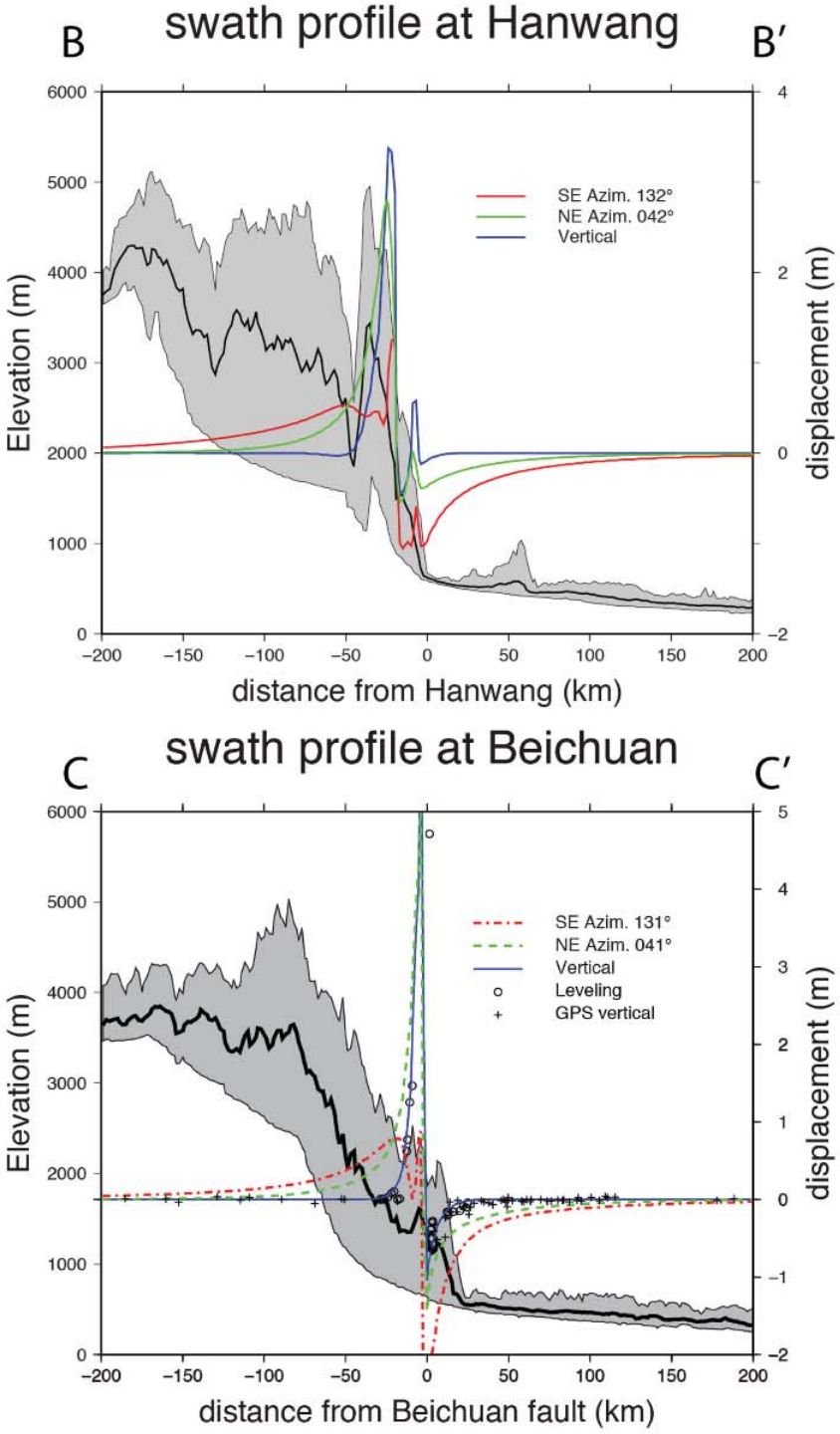

Figure 17. (*Continued.*)

the Himalaya, crystalline rocks with similar resistance to erosion crop out in the High Himalaya farther away, about 100 km from the foreland thrust belt. This is because of the fact that a thick and wide orogenic wedge of sediment detached from the Indian basement has been accreted to the Himalayan front by a combination of forward propagation of the thrust system and underplating (e.g. Avouac 2003). These moderately erodible low-grade metamorphic rocks are not exposed at the front of the Longmen Shan, where only sedimentary rocks have been uplifted by the Pengguan Fault and other thrusts (Hubbard & Shaw 2009; Hubbard *et al.* 2010). It is

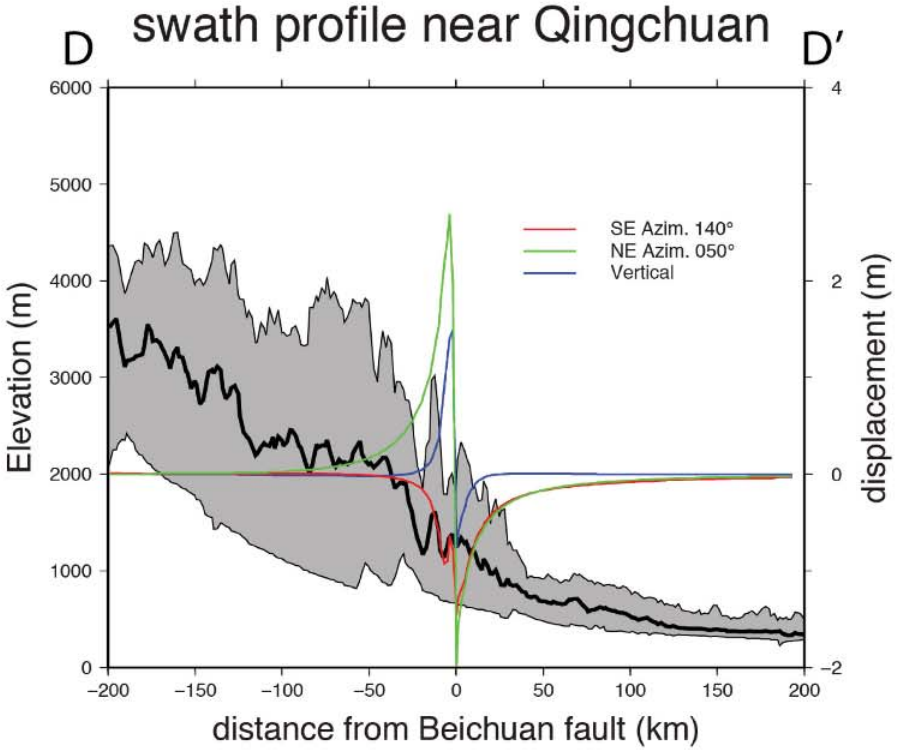

Figure 17. (*Continued.*)

possible, however, that the topography of the Longmen Shan is not at equilibrium with recent tectonic activity. The pattern of erosion (Kirby *et al.* 2003; Godard *et al.* 2010) indeed suggests a transient wave of erosion propagating headwards, which may have originated at the mountain front about 10 Ma ago. So it is possible that relatively low rates of erosion and recent initiation of rapid thrusting along the Longmen Shan mean that no dynamic equilibrium has been reached yet.

5 CONCLUSIONS

The 2008 Wenchuan earthquake ruptured a complex system of faults along the edge of the Tibetan Plateau in the Longmen Shan. The combination of geodetic (GPS), remote-sensing (InSAR and SAR amplitude offsets) and seismological records allows us to describe the source of that earthquake in some detail. The first part of the earthquake was primarily thrust slip on the Beichuan Fault beneath the steep central Longmen Shan, which was followed by slip on the subparallel Pengguan Fault to the southeast. The nearly simultaneous rupture of two faults in an imbricate stack likely involves dynamic triggering, although our teleseismic analysis does not constrain the relative timing of the two ruptures. A deep fault segment beneath eastern Tibet that appears to be a shallowly dipping fault or detachment connected to the southern Beichuan and Pengguan Faults also had significant slip, but the timing of this slip is somewhat uncertain and could be at least in part post-seismic. The earthquake rupture continued to the northeast onto another segment of the Beichuan Fault starting near the city of Beichuan, with oblique thrust and right-lateral slip. Finally, the last fault to rupture to the northeast was nearly pure strike-slip and probably part of the Qingchuan Fault system. The rupture was complex, with significant changes in strike of the main rupture and secondary faults at nearly 90° from the mean strike, and the rupture process lasted some 110 s.

The rotation of the fault slip vectors from thrust to strike-slip during the earthquake also caused a change in the coseismic strain from uplift and southeast-directed shortening in the central Longmen Shan to lateral motion with little uplift in the northeastern Longmen Shan. This change in coseismic strain is consistent with the large-scale geomorphologic characteristics, with an extremely steep mountain front in the central Longmen Shan and much less topographic relief in the northeastern part. This suggests that the 2008 earthquake deformation likely reflects the late Cenozoic tectonics of the Longmen Shan overthrusting the Sichuan Basin lithosphere.

ACKNOWLEDGEMENTS

We thank many researchers for sharing their thoughts on this earthquake, including Zheng-Kang Shen, Jing Liu-Zeng, Judith Hubbard, Chen Ji, Dan McKenzie and Ken Hudnut. We thank Kiran Kumar Thingbaijam for help with formatting our slip model results into the SRCMOD format. Envisat data is copyright European Space Agency and provided under projects AOE-668 and Dragon-2 (ID: 5343). ALOS data is copyright Japanese Aerospace Exploration Agency and METI and provided through the US Government Research Consortium Data Pool at the Alaska Satellite Facility and through ALOS PI project 061. Part of this research was supported by the NASA Earth Surface and Interior focus area and performed at the Jet Propulsion Laboratory, California Institute of Technology, Pasadena. Additional support was provided by the National Science Foundation grant EAR-1014880. This research was funded in part by the Gordon and Betty Moore Foundation through Grant GBMF #423.01 to the Caltech Tectonics Observatory. This work

was supported in part by the Natural Environmental Research Council through the GAS project (Reference: NE/H001085/1), by the National Centre of Earth Observation of which the Centre for the Observation and Modelling of Earthquakes, Volcanoes, and Tectonics (COMET+) is a part. Caltech Tectonics Observatory Contribution 227.

REFERENCES

Avouac, J.P., 2003. Mountain building, erosion, and the seismic cycle in the Nepal Himalaya, *Adv. Geophys.*, **46,** 1–80.

Avouac, J.P., Ayoub, F., Leprince, S., Konca, O. & Helmberger, D.V., 2006. The 2005, Mw 7.6 Kashmir earthquake: sub-pixel correlation of ASTER images and seismic waveforms analysis, *Earth planet. Sci. Lett.*, **249,** 514–528.

Bamler, R. & Eineder, M., 1996. ScanSAR processing using standard high precision SAR algorithms, *IEEE Trans. Geosci. Remote Sens.*, **34,** 212–218.

Bassin, C., Laske, G. & Masters, G., 2000. The current limits of resolution for surface wave tomography in North America, *Eos Trans. AGU,* **81,** Fall Meet. Suppl., Abstract S12A-03.

Burchfiel, B.C. *et al.*, 2008. A geological and geophysical context for the Wenchuan earthquake of 12 May 2008, Sichuan, People's Republic of China, *GSA Today,* **18,** 4–11.

Burchfiel, B.C., Zhiliang, C., Yupinc, L. & Royden, L.H., 1995. Tectonics of the Longmen Shan and Adjacent Regions, Central China, *Int. Geol. Rev.,* **37,** 661–735.

Chen, C.W. & Zebker, H.A., 2002. Phase unwrapping for large SAR interferograms: statistical segmentation and generalized network models, *IEEE Trans. Geosci. Remote Sens.*, **40,** 1709–1719.

Chen, Z. *et al.*, 2000. Global Positioning System measurements from eastern Tibet and their implications for India/Eurasia intercontinental deformation, *J. geophys. Res.,* **105,** 16215–16227.

Danielson, J.J. & Gesch, D.B., 2011. *Global Multi-resolution Terrain Elevation Data 2010 (GMTED2010),* U.S. Geological Survey, Reston, Virginia, p. 26.

de Michele, M., Raucoules, D., De Sigoyer, J., Pubellier, M. & Chamot-Rooke, N., 2010a. Three-dimensional surface displacement of the 2008 May 12 Sichuan earthquake (China) derived from Synthetic Aperture Radar: evidence for rupture on a blind thrust, *Geophys. J. Int.,* **183,** 1097–1103.

de Michele, M., Raucoules, D., Lasserre, C., Pathier, E., Klinger, Y., Van der Woerd, J., de Sigoyer, J. & Xu, X.W., 2010b. The M-w 7.9, 12 May 2008 Sichuan earthquake rupture measured by sub-pixel correlation of ALOS PALSAR amplitude images, *Earth planets Space,* **62,** 875–879.

Delouis, B., Lundgren, P., Salichon, J. & Giardini, D., 2000. Joint inversion of InSAR and teleseismic data for the slip history of the 1999 Izmit (Turkey) earthquake, *Geophys. Res. Lett.*, **27,** 3389–3392.

Densmore, A.L., Ellis, M.A., Li, Y., Zhou, R., Hancock, G.S. & Richardson, N., 2007. Active tectonics of the Beichuan and Pengguan faults at the eastern margin of the Tibetan Plateau, *Tectonics,* **26,** TC4005, doi:10.1029/2006TC001987.

Engdahl, E.R., van der Hilst, R. & Buland, R., 1998. Global teleseismic earthquake relocation with improved travel times and procedures for depth determination, *Bull. seism. Soc. Am.*, **88,** 722–743.

Farr, T.G. *et al.*, 2007. The Shuttle Radar Topography Mission, *Rev. Geophys.*, **45,** RG2004, doi:10.1029/2005RG000183.

Feng, G., Hetland, E.A., Ding, X., Li, Z. & Zhang, L., 2010. Coseismic fault slip of the 2008 Mw 7.9 Wenchuan earthquake estimated from InSAR and GPS measurements, *Geophys. Res. Lett.*, **37,** L01302, doi:10.1029/2009GL041213.

Fielding, E.J., 1996. Tibet uplift and erosion, *Tectonophysics,* **260,** 55–84.

Fielding, E.J. & McKenzie, D., 2012. Lithospheric flexure in the Sichuan Basin and Longmen Shan at the eastern edge of Tibet, *Geophys. Res. Lett.,* **39,** L09311, doi:10.1029/2012GL051680.

Furuya, M., Kobayashi, T., Takada, Y. & Murakami, M., 2010. Fault Source Modeling of the 2008 Wenchuan Earthquake Based on ALOS/PALSAR Data, *Bull. seism. Soc. Am.*, **100,** 2750–2766.

Godard, V., Lavé, J., Carcaillet, J., Cattin, R., Bourlès, D. & Zhu, J., 2010. Spatial distribution of denudation in Eastern Tibet and regressive erosion of plateau margins, *Tectonophysics,* **491,** 253–274.

Goldstein, R.M. & Werner, C.L., 1998. Radar interferogram filtering for geophysical applications, *Geophys. Res. Lett.*, **25,** 4035–4038.

Gray, A.L., Mattar, K.E. & Sofko, G., 2000. Influence of ionospheric electron density fluctuations on satellite radar interferometry, *Geophys. Res. Lett.,* **27,** 1451–1454.

Hayes, G.P. *et al.*, 2010. Complex rupture during the 12 January 2010 Haiti earthquake, *Nat. Geosci.,* **3,** 800–805.

Hernandez, B., Cotton, F. & Campillo, M., 1999. Contribution of radar interferometry to a two-step inversion of the kinematic process of the 1992 Landers earthquake, *J. geophys. Res.,* **104,** 13 083–13 099.

Hubbard, J. & Shaw, J.H., 2009. Uplift of the Longmen Shan and Tibetan plateau, and the 2008 Wenchuan (M = 7.9) earthquake, *Nature,* **458,** 194–197.

Hubbard, J., Shaw, J.H. & Klinger, Y., 2010. Structural Setting of the 2008 Mw 7.9 Wenchuan, China, Earthquake, *Bull. seism. Soc. Am.*, **100,** 2713–2735.

Jarvis, A., Reuter, H.I., Nelson, A. & Guevara, E., 2008. Hole-filled seamless SRTM data V4 International Centre for Tropical Agriculture (CIAT). Available at: http://srtm.csi.cgiar.org/. Last accessed 1 May 2013.

Ji, C. & Hayes, G., 2008. Finite fault model: preliminary result of the May 12, 2008 Mw 7.9 Eastern Sichuan, China Earthquake. Available at: http://earthquake.usgs.gov/earthquakes/eqinthenews/2008/us2008ryan/finite_fault.php. Last accessed 30 April 2013.

Ji, C., Helmberger, D.V., Song, T.-R.A., Ma, K.-F. & Wald, D.J., 2001. Slip distribution and tectonic implication of the 1999 Chi-Chi, Taiwan, Earthquake, *Geophys. Res. Lett.,* **28,** 4379–4382.

Ji, C., Wald, D.J. & Helmberger, D.V., 2002. Source Description of the 1999 Hector Mine, California, Earthquake, Part I: WAVELET Domain Inversion Theory and Resolution Analysis, *Bull. seism. Soc. Am.*, **92,** 1192–1207.

Jiang, X.D. & Jin, Y., 2005. Mapping the deep lithospheric structure beneath the eastern margin of the Tibetan Plateau from gravity anomalies, *J. geophys. Res.-Solid Earth,* **110,** B07407, doi:10.1029/2004JB003394.

Jones, L.M., Han, W.B., Hauksson, E., Jin, A.S., Zhang, Y.G. & Luo, Z.L., 1984. Focal mechanisms and aftershock locations of the Songpan earthquakes of August 1976 in Sichuan, China, *J. geophys. Res.*, **89,** 7697–7707.

Kirby, E., Whipple, K. & Harkins, N., 2008. Topography reveals seismic hazard, *Nat. Geosci.,* **1,** 485–487.

Kirby, E., Whipple, K.X., Burchfiel, B.C., Tang, W.Q., Berger, G., Sun, Z.M. & Chen, Z.L., 2000. Neotectonics of the Min Shan, China: implications for mechanisms driving Quaternary deformation along the eastern margin of the Tibetan Plateau, *Bull. geol. Soc. Am.*, **112,** 375–393.

Kirby, E., Whipple, K.X., Tang, W.Q. & Chen, Z.L., 2003. Distribution of active rock uplift along the eastern margin of the Tibetan Plateau: inferences from bedrock channel longitudinal profiles, *J. geophys. Res.*, **108,** 2217, doi:10.1029/2001JB000861.

Klinger, Y., Xu, X.W., Tapponnier, P., Van der Woerd, J., Lasserre, C. & King, G., 2005. High-resolution satellite imagery mapping of the surface rupture and slip distribution of the Mw ~ 7.8, 14 November 2001 Kokoxili Earthquake, Kunlun Fault, northern Tibet, China, *Bull. seism. Soc. Am.*, **95,** 1970–1987.

Kobayashi, T., Takada, Y., Furuya, M. & Murakami, M., 2009. Locations and types of ruptures involved in the 2008 Sichuan earthquake inferred from SAR image matching, *Geophys. Res. Lett.*, **36,** L07302, doi:10.1029/2008GL036907.

Konca, A.O., Leprince, S., Avouac, J.P. & Helmberger, D.V., 2010. Rupture process of the 1999 Mw 7.1 Duzce Earthquake from joint analysis of SPOT, GPS, InSAR, strong-motion, and teleseismic data: a supershear rupture with variable rupture velocity, *Bull. seism. Soc. Am.*, **100,** 267–288.

Kuo, Y., Huang, M., Suppe, J., Chen, Y., Avouac, J., Leprince, S. & Ayoub, F., 2008. Coseismic ground displacements from sub-pixel correlation for the 2008 Wenchuan Earthquake, Sichuan, China, *EOS, Trans. Am. geophys. Un.*, **89,** Fall Meet. Suppl., Abstract U23B-0057.

Li, Y. *et al.*, 2010. Structural interpretation of the coseismic faults of the Wenchuan earthquake: three-dimensional modeling of the Longmen Shan fold-and-thrust belt, *J. geophys. Res.,* **115,** B04317, doi:10.1029/2009JB006824.

Lin, A.M., Ren, Z.K., Jia, D. & Wu, X.J., 2009. Co-seismic thrusting rupture and slip distribution produced by the 2008 M-w 7.9 Wenchuan earthquake, China, *Tectonophysics,* **471,** 203–215.

Liu-Zeng, J., Wen, L., Oskin, M. & Zeng, L., 2011. Focused modern denudation of the Longmen Shan margin, eastern Tibetan Plateau, *Geochem. Geophys. Geosyst.,* **12,** Q11007, doi:10.1029/2011GC003652.

Liu-Zeng, J. *et al.*, 2009. Co-seismic ruptures of the 12 May, 2008, M_S 8.0 Wenchuan earthquake, Sichuan: east-west crustal shortening on oblique, parallel thrusts along the eastern edge of Tibet, *Earth planet. Sci. Lett.*, **286,** 355–370.

Lohman, R.B. & Simons, M., 2005. Some thoughts on the use of InSAR data to constrain models of surface deformation: noise structure and data downsampling, *Geochem. Geophys. Geosyst.,* **6,** Q01007, doi:10.1029/2004GC000841.

Manighetti, I., Campillo, M., Sammis, C., Mai, P.M. & King, G., 2005. Evidence for self-similar, triangular slip distributions on earthquakes: Implications for earthquake and fault mechanics, *J. geophys. Res.*, **110,** B05302, doi:10.1029/2004JB003174.

Meyer, F., Bamler, R., Jakowski, N. & Fritz, T., 2006. The potential of low-frequency SAR systems for mapping ionospheric TEC distributions, *IEEE Geosci. Remote Sens. Lett.,* **3,** 560–564.

Meyer, F. & Nicoll, J., 2008. The Impact of the Ionosphere on Interferometric SAR Processing, in *IEEE International Geoscience and Remote Sensing Symposium,* pp. II-391–II-394, IEEE, Boston, MA.

Michel, R., Avouac, J.-P. & Taboury, J., 1999. Measuring ground displacements from SAR amplitude images: application to the Landers earthquake, *Geophys. Res. Lett.*, **26,** 875–878.

Monti Guarnieri, A. & Prati, C., 1996. ScanSAR focusing and interferometry, *IEEE Trans. Geosci. Remote Sens.,* **34,** 1029–1038.

Pathier, E., Fielding, E.J., Wright, T.J., Walker, R., Parsons, B.E. & Hensley, S., 2006. Displacement field and slip distribution of the 2005 Kashmir earthquake from SAR imagery, *Geophys. Res. Lett.*, **33,** L20310, doi:10.1029/2006GL027193.

Raucoules, D. & de Michele, M., 2010. Assessing ionospheric influence on L-band SAR data: implications on coseismic displacement measurements of the 2008 Sichuan earthquake, *IEEE Geosci. Remote Sens. Lett.,* **7,** 286–290.

Replumaz, A. & Tapponnier, P., 2003. Reconstruction of the deformed collision zone Between India and Asia by backward motion of lithospheric blocks, *J. geophys. Res.*, **108,** 2285, doi:10.1029/2001JB000661.

Rosen, P.A., Hensley, S., Peltzer, G. & Simons, M., 2004. Updated repeat orbit interferometry package released, *EOS, Trans. Am. geophys. Un.*, **85,** 47.

Royden, L.H., Burchfiel, B.C., King, R.W., Wang, E., Chen, Z., Shen, F. & Liu, Y., 1997. Surface deformation and lower crustal flow in eastern Tibet, *Science,* **276,** 788–790.

Royden, L.H., Burchfiel, B.C. & van der Hilst, R.D., 2008. The geological evolution of the Tibetan Plateau, *Science,* **321,** 1054–1058.

Ryder, I., Bürgmann, R. & Sun, J., 2010. Tandem afterslip on connected fault planes following the 2008 Nima-Gaize (Tibet) earthquake, *J. geophys. Res.*, **115,** B03404, doi:10.1029/2009JB006423.

Salichon, J., Delouis, B., Lundgren, P., Giardini, D., Costantini, M. & Rosen, P., 2003. Joint inversion of broadband teleseismic and interferometric synthetic aperture radar (InSAR) data for the slip history of the Mw = 7.7, Nazca ridge (Peru) earthquake of 12 November 1996, *J. geophys. Res.,* **108,** 2085, doi:10.1029/2001JB000913.

Segall, P. & Pollard, D.D., 1980. Mechanics of discontinuous faults, *J. geophys. Res.*, **85,** 4337–4350.

Shen, Z.K., Lü, J., Wang, M. & Bürgmann, R., 2005. Contemporary crustal deformation around the southeast borderland of the Tibetan Plateau, *J. geophys. Res.,* **110,** B11409, doi:10.1029/2004JB003421.

Shen, Z.K. *et al.*, 2009. Slip maxima at fault junctions and rupturing of barriers during the 2008 Wenchuan earthquake, *Nat. Geosci.,* **2,** 718–724.

Sibson, R.H., 1985. Stopping of earthquake ruptures at dilational fault jogs, *Nature,* **316,** 248–251.

Sladen, A. *et al.*, 2010. Source model of the 2007 Mw 8.0 Pisco, Peru earthquake–implications for seismogenic behavior of subduction megathrusts, *J. geophys. Res.,* **115,** B02405, doi:10.1029/2009JB006429.

Sun, Y.S., Kuleli, S., Morgan, F.D., Rodi, W., Toksoz, M.N., Han, W.B. & Lu, Z.Y., 2004. Location robustness of earthquakes in Sichuan Province, China, *Seism. Res. Lett.,* **75,** 54–62.

Tong, X., Sandwell, D.T. & Fialko, Y., 2010. Coseismic slip model of the 2008 Wenchuan earthquake derived from joint inversion of interferometric synthetic aperture radar, GPS, and field data, *J. geophys. Res.,* **115,** B04314, doi:10.1029/2009JB006625.

Wang, Q., Cui, D., Zhang, X., Wang, W., Liu, J., Tian, K. & Song, Z., 2009. Coseismic vertical deformation of the M_S 8.0 Wenchuan earthquake from repeated levelings and its constraint on listric fault geometry, *Earthq. Sci.,* **22,** 595–602.

Wang, Q. *et al.*, 2011. Rupture of deep faults in the 2008 Wenchuan earthquake and uplift of the Longmen Shan, *Nat. Geosci.,* **4,** 634–640.

Wei, S. *et al.*, 2011. Superficial simplicity of the 2010 El Mayor–Cucapah earthquake of Baja California in Mexico, *Nat. Geosci.,* **4,** 615–618.

Wei, S., Graves, R., Helmberger, D., Avouac, J.-P. & Jiang, J., 2012. Sources of shaking and flooding during the Tohoku-Oki earthquake: a mixture of rupture styles, *Earth planet. Sci. Lett.*, **333,** 91–100.

Wen, Y.-Y., Ma, K.-F. & Oglesby, D.D., 2012. Variations in rupture speed, slip amplitude and slip direction during the 2008 Mw 7.9 Wenchuan Earthquake, *Geophys. J. Int.,* **190,** 379–390.

Wesnousky, S.G., 2006. Predicting the endpoints of earthquake ruptures, *Nature,* **444,** 358–360.

Working Group of the Crustal Motion Observation Network of China Project, 2008. The coseismic displacement of 2008 Wenchuan Ms 8.0 earthquake measured by GPS (in Chinese), *Science in China, Series D,* **38,** 1195–1206.

Xu, X.W., Wen, X.Z., Chen, G.H. & Yu, G.H., 2008a. Discovery of the Longriba fault zone in eastern Bayan Har block, China and its tectonic implication, *Sci. China,* **51,** 1209–1223.

Xu, Z.Q., Ji, S.C., Li, H.B., Hou, L.W., Fu, X.F. & Cai, Z.H., 2008b. Uplift of the Longmen Shan range and the Wenchuan earthquake, *Episodes,* **31,** 291–301.

Xu, X.W., Wen, X.Z., Yu, G.H., Chen, G.H., Klinger, Y., Hubbard, J. & Shaw, J., 2009a. Coseismic reverse- and oblique-slip surface faulting generated by the 2008 Mw 7.9 Wenchuan earthquake, China, *Geology,* **37,** 515–518.

Xu, Y., Koper, K.D., Sufri, O., Zhu, L.P. & Hutko, A.R., 2009b. Rupture imaging of the M-w 7.9 12 May 2008 Wenchuan earthquake from back projection of teleseismic P waves, *Geochem. Geophys. Geosyst.,* **10,** Q04006, doi:10.1029/2008GC002335.

Xu, C., Liu, Y., Wen, Y. & Wang, R., 2010. Coseismic slip distribution of the 2008 Mw 7.9 Wenchuan earthquake from joint inversion of GPS and InSAR data, *Bull. seism. Soc. Am.*, **100,** 2736–2749.

Zhang, G., Qu, C., Shan, X., Song, X., Zhang, G., Wang, C., Hu, J.-C. & Wang, R., 2011. Slip distribution of the 2008 Wenchuan Ms 7.9 earthquake by joint inversion from GPS and InSAR measurements: a resolution test study, *Geophys. J. Int.,* **186,** 207–220.

Zhang, H. & Ge, Z.X., 2010. Tracking the rupture of the 2008 Wenchuan Earthquake by using the relative back-projection method, *Bull. seism. Soc. Am.*, **100,** 2551–2560.

Zhang, P.-Z., Wen, X.-Z., Shen, Z.-K. & Chen, J.-H., 2010. Oblique, high-angle, listric-reverse faulting and associated development of strain: the Wenchuan Earthquake of May 12, 2008, Sichuan, China, *Ann. Rev. Earth planet. Sci.,* **38,** 353–382.

Zhang, P.Z., Xu, X.W., Wen, X.Z. & Ran, Y.K., 2008. Slip rates and recurrence intervals of the Longmen Shan active fault zone, and tectonic implications for the mechanism of the May 12 Wenchuan earthquake, 2008, Sichuan, China, *Chinese J. Geophys.-Ch.,* **51,** 1066–1073.

Zhang, Z., Wang, Y., Chen, Y., Houseman, G.A., Tian, X., Wang, E. & Teng, J., 2009. Crustal structure across Longmenshan fault belt from passive source seismic profiling, *Geophys. Res. Lett.*, **36,** L17310, doi:10.1029/2009GL039580.

Zhou, R.J., Li, Y., Densmore, A.L., Ellis, M.A., He, Y.L., Li, Y.Z. & Li, X.G., 2007. Active tectonics of the Longmen Shan region on the eastern margin of the Tibetan plateau, *Acta Geol. Sin.-Engl. Ed.,* **81,** 593–604.

SUPPORTING INFORMATION

Additional Supporting Information may be found in the online version of this article:

Figure S1. Maps of down-sampled interferograms, with sampled line-of-sight range change values plotted over the area of the quadrangle averaged for that sample. Positive range change means motion away from the satellite. Sampling was done using the Lohman & Simons (2005) quad-tree method to optimize resolution of slip on the faults of the Longmenshan. Note that the colour scale is different for each interferogram to make it easier to see the details despite large variations of total range change between interferograms. (a) ALOS fine-beam interferograms from ascending paths 470–477, six of which have been masked to only keep the area of large deformation where the earthquake signal is larger than the ionospheric noise (dashed polygon on Fig. 2 of main text). (b) Envisat image mode interferograms and Envisat wide-swath (ScanSAR) interferogram on descending tracks (see also Fig. 3 of main text) (c) ALOS wide-beam (ScanSAR) interferogram from descending path 124 (see also Fig. 5 of main text).

Figure S2. Checkerboard test for static slip inversion of GPS and InSAR data. (a) Synthetic slip model with 3 × 3 subfault (30 × 12 km) checkerboard pattern. (b) Slip model from static inversion of checkerboard synthetic data. (c) Map view of final slip of checkerboard slip inversion superimposed on a topographic map, similar to Fig. 10 of main text. Coloured rectangles show slip distribution. Black arrows show synthetic GPS horizontal observations and gray arrows show synthetic vertical observations. Red arrows show horizontal prediction and green arrows show vertical prediction of our model from geodetic inversion of InSAR and GPS data.

Figure S3. Maps of InSAR data after ramp removal (left), static model prediction from geodetic-only inversion (shown in Fig. 9 of main text) projected into radar LOS (centre), and difference between data and model (right), with annotation similar to Fig. 16 of main text. (a) Wrapped interferograms, where the LOS motion has been rewrapped with a 12 cm colour cycle. Interferogram tracks are listed in each row. (b) Unwrapped interferograms where the colour scale is continuous with a range between −80 and 80 cm.

Figure S4. (a) Map view of final displacements of teleseismic-only slip model superimposed on a topographic map, similar to Fig. 12 of main text. Coloured rectangles show slip distribution. Black arrows show GPS observations from Wang *et al.* (2011) and red arrows show prediction of our preferred model from joint inversion of teleseismic, InSAR and GPS data. Dashed outline box shows area plotted in (e). (b) Profile along Beichuan Fault showing offsets measured in the field (green) (Lin *et al.* 2009) and (blue) (Liu-Zeng *et al.* 2009). Red line shows total slip in the top 4 by 4 km patch of preferred model. (c) Map view of field surface rupture measurement locations (green and blue dots) on rupture lines mapped from SAR subpixel correlation (orange lines). (d) Profile of field offset measurements along Pengguan Fault with same symbols as (b). (e) Levelling profile measurements and model predictions on detail map of central area. Red bars show vertical displacements from levelling profiles (Wang *et al.* 2009), and black bars show our model predictions.

Figure S5. Maps of InSAR data after ramp removal (left), final slip model prediction from teleseismic-only inversion projected into radar LOS (centre), and difference between data and model (right), similar to Fig. 16 of main text. (a) Wrapped interferograms, where the LOS motion has been rewrapped with a 12 cm colour cycle. Interferogram tracks are listed in each row. (b) Unwrapped interferograms where the colour scale is continuous with a range between −80 and 80 cm. (c) Fits to teleseismic waveforms, similar to Fig. 13 of main text.

Figure S6. Map views of final displacements from preferred kinematic slip model of joint inversion. Black lines show fault ruptures, black outline star is USGS epicentre and black filled star is our epicentre. Black rectangles show surface projections of fault segments. (a) Vertical displacements. (b) Southeast displacements (azimuth 131°) normal to Beichuan Fault. (c) Northeast displacements (azimuth 41°) parallel to Beichuan Fault.

Table S1. Source model from geodetic-only inversion in Finite Source Parameter (FSP) format, as used in the SRCMOD database (http://equake-rc.info/srcmod/).

Table S2. Source model from teleseismic-only inversion in FSP format.

Table S3. Source model from preferred joint inversion in FSP format. (http://gji.oxfordjournals.org/lookup/suppl/doi:10.1093/gji/ggt155/-/DC1).

Please note: Oxford University Press are not responsible for the content or functionality of any supporting materials supplied by the authors. Any queries (other than missing material) should be directed to the corresponding author for the article.